

Article

Assessment of Tire Features for Modeling Vehicle Stability in Case of Vertical Road Excitation

Vaidas Lukoševičius *, Rolandas Makaras  and Andrius Dargužis

Faculty of Mechanical Engineering and Design, Kaunas University of Technology, Studentų Str. 56, 44249 Kaunas, Lithuania; rolandas.makaras@ktu.lt (R.M.); andrius.darguzis@ktu.lt (A.D.)

* Correspondence: vaidas.lukosevicius@ktu.lt

Abstract: Two trends could be observed in the evolution of road transport. First, with the traffic becoming increasingly intensive, the motor road infrastructure is developed; more advanced, greater quality, and more durable materials are used; and pavement laying and repair techniques are improved continuously. The continued growth in the number of vehicles on the road is accompanied by the ongoing improvement of the vehicle design with the view towards greater vehicle controllability as the key traffic safety factor. The change has covered a series of vehicle systems. The tire structure and materials used are subject to continuous improvements in order to provide the maximum possible grip with the road pavement. New solutions in the improvement of the suspension and driving systems are explored. Nonetheless, inevitable controversies have been encountered, primarily, in the efforts to combine riding comfort and vehicle controllability. Practice shows that these systems perform to a satisfactory degree only on good quality roads, as they have been designed specifically for the latter. This could be the cause of the more complicated car control and accidents on the lower-quality roads. Road ruts and local unevenness that impair car stability and traffic safety are not avoided even on the trunk roads. In this work, we investigated the conditions for directional stability, the influence of road and vehicle parameters on the directional stability of the vehicle, and developed recommendations for the road and vehicle control systems to combine to ensure traffic safety. We have developed a refined dynamic model of vehicle stability that evaluates the influence of tire tread and suspensions. The obtained results allow a more accurate assessment of the impact of the road roughness and vehicle suspension and body movements on vehicle stability and the development of recommendations for the safe movement down the road of known characteristics.

Keywords: directional stability; road profile; road unevenness; vehicle-road interaction; vertical vehicle excitation; tire models; tire tread



Citation: Lukoševičius, V.; Makaras, R.; Dargužis, A. Assessment of Tire Features for Modeling Vehicle Stability in Case of Vertical Road Excitation. *Appl. Sci.* **2021**, *11*, 6608. <https://doi.org/10.3390/app11146608>

Academic Editors: Flavio Farroni, Andrea Genovese and Aleksandr Sakhnevych

Received: 29 June 2021
Accepted: 16 July 2021
Published: 18 July 2021

Publisher's Note: MDPI stays neutral with regard to jurisdictional claims in published maps and institutional affiliations.



Copyright: © 2021 by the authors. Licensee MDPI, Basel, Switzerland. This article is an open access article distributed under the terms and conditions of the Creative Commons Attribution (CC BY) license (<https://creativecommons.org/licenses/by/4.0/>).

1. Introduction

The vehicle-road subsystem includes various aspects of the vehicle-road interaction. This subsystem is emphasized where the technical part of transport operations is investigated. Considerable emphasis has already been placed on the description of the vehicle-road interaction, vehicle movement under various conditions, and substantiation of the requirements for vehicles both in the theoretical studies and in the experimental investigations where the theory has not provided any viable solutions [1–3]. Basic solutions could mistakenly be considered to have been found, with further inquiry allegedly being limited to observations that are necessary to correct the solutions. Nonetheless, certain limitations have been introduced increasingly by a lot of countries in response to the aggressive development of this type of transport. These limitations have an effect both on individual components of the subsystem and on the subsystem itself and promote the improvement of both technical and organizational aspects thereof. The road and vehicle as the elements of the vehicle-road subsystem may be described individually as they are viewed and may be explored as individual elements of the system in an investigation of transport systems [4].

Pavement unevenness values are not completely random. An attempt was made to systematize these values. A method enabling assessment of the unevenness height dispersion and correlation function that has been used for a fairly long time is already more appropriate for the modeling [5–8]. The specifics of unevenness lie in that certain patterns between the unevenness height and unevenness wavelength become established during the pavement laying process and use. Hence, the random process model cannot be applied to the road description, as waviness and ruts are registered in the road pavement, in particular, after the use [9–12].

In the stability tasks, two types of unevenness have the greatest effect: road micro-profile that causes excitation of the suspension operation [13,14] and road roughness due to its relation to the grip ratio [15–17]. The vehicle-road interaction is determined by two intermediate links: the tire and the suspension [18,19].

Vehicle stability modeling tasks involve multiple parameters and need to be split into several individual tasks during the analysis. Nonetheless, a more detailed inquiry has shown that the tasks are interrelated, and integrated analysis is needed when dealing with more complex tasks. Analysis of the evolution of trends in traffic accidents and vehicle design has shown that controllability is one of the key operational properties of a vehicle that influences safety. Vehicle controllability is the ability to move following the trajectory designed by the driver [20,21]. The driver sets the desired direction using the steering wheel mechanism, and the controllability tasks are focused on the steering wheel mechanism [22,23].

Deeper inquiry into the potential excitation caused by road unevenness has shown that it is not enough to know the slip characteristics, as the wheel direction vector is influenced by the wheel spatial position, i.e., camber, toe alignment, etc. The dynamic equations cannot be used directly due to the specifics of the tasks and to the fact that the characteristics of individual elements are clearly nonlinear. Semi-empirical formulae are used to describe the effect of the change of the forces acting on the wheel and the spatial position thereof on the direction vector. Dependencies of the link between the slip angle and lateral force, lateral force and relative wheel slippage, slip angle, and stabilizing moment are required in order to be able to perform the modeling. During the modeling, the dependencies are expressed by either linear or higher-degree dependencies [24–30].

The majority of the currently available methodologies employ simplified models. These models individually assess the kinematics of the steering wheel mechanism, suspension kinematics, stiffness of the suspension elements, and forces acting on the vehicle while making a turn [31–35]. This kind of analysis does not enable the identification of the key factors. Hence, the models consisting of multiple elements, the characteristics of which can be known only after specific vehicle design details are available, need to be used for the integrated analysis. This complicates the integrated analysis and generalization in the investigation of directional stability viewed as the criterion for assessment of the technical condition of the vehicle and the condition of the pavement. Hence, the focus was first turned to another driver-vehicle-road system element, i.e., road, prior to designing the integrated directional stability model for the vehicle and performing the analysis. In this context, the road is associated with the effects which may cause vehicle instability, while the purpose of improvement of stability is related to the solution of the vehicle-road interaction.

A moving vehicle is subject to external effects and reacts to the driver's actions (Figure 1). In the investigation of vehicle directional stability, all these factors need to be considered. However, the vehicle model becomes very complex, making the analysis of the effect of individual factors more difficult. The present paper does not account for the driver's actions, environmental impact, aerodynamic effects, and vehicles design features.

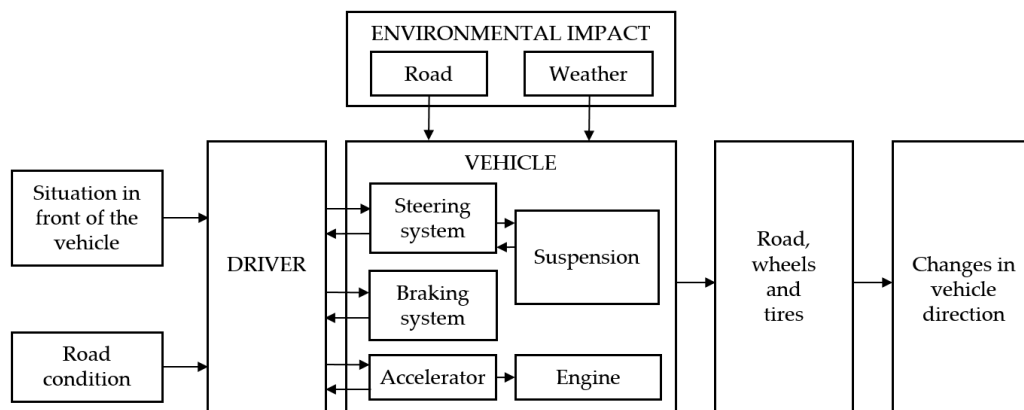


Figure 1. Influence of external factors on vehicle directional stability.

This paper provided a comprehensive review of the key parameters of road-vehicle interaction that have an effect on vehicle stability and design the movement model, consisting of a finite number of parameters, for investigation of stability. The required tire parameters were determined and revised using the theoretical and experimental methods. Following the numerical investigation using the dynamic models, experimental studies were performed to verify the model. The effect of the road parameters on the driving characteristics of the vehicle was investigated. A revised dynamic model of the vehicle directional stability was developed assessing the effect of vehicle suspensions on vehicle stability and traffic safety. The generated results have enabled a more accurate assessment of the influence of road unevenness and vehicle tire and car body vibrations on vehicle stability, and the development of the recommendations on safe movement on the roads using the available characteristics.

Based on the topics discussed above, the main contributions of this paper are as follows: (1) we examine the vehicle stability dynamic models and develop a refined methodology for estimating the key parameters of these models; (2) we produce a revised tire smoothing function model that takes into account tread deflections; (3) we investigate vertical dynamics models and develop recommendations for their use in-vehicle stability studies; (4) we verify the validity of the model of the vertical dynamics using experimental studies; and (5) we establish the vehicle stability model, allowing evaluation of vehicles' technical performance and safe driving conditions of vehicles on roads with different characteristics.

2. Investigation the Tire-Road Interaction

2.1. Investigation of the Tire Properties

When dealing with the vehicle stability tasks, the issue of tire-road interaction is one of the most complex tasks. Analysis of the vehicle wheel-to-road contact requires taking into account the deformation properties of the tire. The complexity of the task stems from the uncertainty of the operating conditions of the tire and the complex structure of the tire. The complexity of the problem is defined by the mere fact that no consensus has been reached on the shape of the tire.

The performed studies of the tire-road interaction [36] confirmed that it would be necessary to consider the deformation properties of the band in the investigation of the compensating function of the band. For this purpose, an additional element is added to the quarter-car model (Figure 2). Additional studies are needed in order to identify the deformation properties of the element.

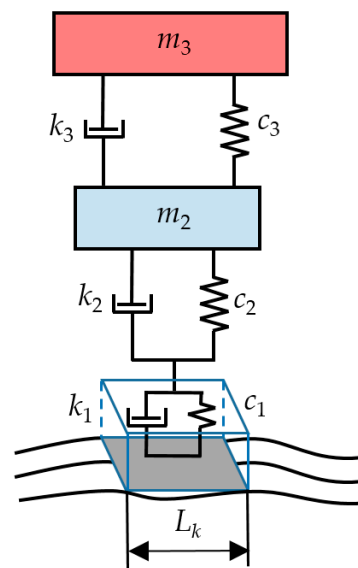


Figure 2. Quarter-car model: L_k —tire-road contact length; m_1 , c_1 and k_1 —mass, stiffness, and damping ratio of the tire tread part; c_2 , k_2 —tire stiffness and damping ratio; c_3 , k_3 —suspension stiffness and damping ratio; m_2 —unsprung mass; m_3 —sprung mass.

The methodology may be used where deformation of an additional element, i.e., the tread, is needed in the quarter-car model (Figure 2). Whereas both tread layers (with and without the pattern) are not made of composite material, the equations applicable to rubber parts are used here as they consider that $\nu = 0.5$ [37]. The tread model is comprised of two consistently joined layers: the one with a pattern and the one without a pattern. The deformation of the part with a pattern was assessed using three models.

This paper analyzes radial tires of three types that differ considerably in terms of structure: passenger car (175/70R13; 195/50R15), light-duty truck (185/75R14C), and heavy-duty truck (12.00R20) tires. In the assessment of the vehicle tire-road interaction, it is first necessary to describe the deformation properties of the tire under the vertical load. The static load consists of the vehicle and cargo mass. The loaded tire is subject to deformation when forming the contact area with the road pavement. The tire-road contact is depicted in Figure 3, and tire element characteristics are presented in Table 1. The following assumptions were used when determining the area of the contact with the road:

- the contact with the road has an elliptical shape and is limited by the tire width and length of the contact with the road;
- the layers under the tread are sufficiently stiff, and their length does not change during deformation of the tire ($l_d \approx l_0$) (Figure 3a);
- there is the linear dependency between the radial load of the tire and radial deformation Δh ;
- the pressure is distributed evenly across the contact surface.

The second and third assumptions enable determining the length of the tire-road contact:

$$L_k/2 = r \cdot \arccos((1 - C_R R_z)/r) \quad (1)$$

where C_R —radial stiffness of the tire and r —free radius of the tire.

More accurate information on the tire element loads is provided by the model ‘elastic ring with the outer elastic layer’ (Figure 4a,b) [38]. The ring is considered to be the elastic band; the tensile force N_0 caused within it by the inner pressure does not change during deformation; and the ring points are displaced only in the radial direction by the measure w .

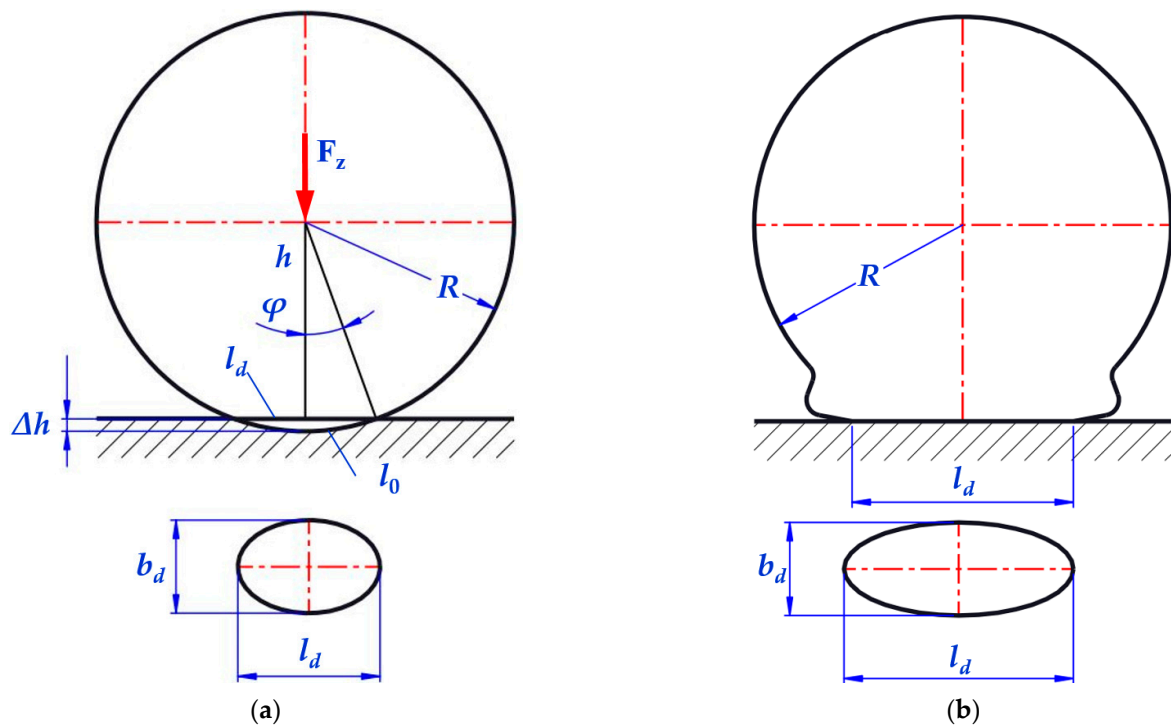


Figure 3. Tire load scheme: (a) tire deformation not assessed; (b) tire deformation assessed.

Table 1. Data of the tire components.

	Tire	Tire Element	
		Thickness, mm	Fiber Angle
A	175/70R13 Breaker, 3 layers Cord, 1 layer	$\delta_{1a} = 8.0$	–
		$\delta_{1b} = 7.0$	–
		$\delta_2 = 4.1$	$\theta_2 = 20^\circ$
		$\delta_3 = 1.2$	$\theta_3 = 90^\circ$
		$\delta_4 = 1.0$	–
B	195/50R15 Breaker, 2 layers Cord, 2 layers	$\delta_{1a} = 8.1$	–
		$\delta_{1b} = 7.8$	–
		$\delta_2 = 3.9$	$\theta_2 = 20^\circ$
		$\delta_3 = 1.7$	$\theta_3 = 90^\circ$
		$\delta_4 = 1.3$	–
C	185/75R14C Breaker, 2 layers Cord, 2 layers	$\delta_{1a} = 12.0$	–
		$\delta_{1b} = 11.0$	–
		$\delta_2 = 3.2$	$\theta_2 = 20^\circ$
		$\delta_3 = 1.8$	$\theta_3 = 90^\circ$
		$\delta_4 = 1.0$	–
D	12.00R20 Breaker, 4 layers Cord, 6 layers	$\delta_{1a} = 17.0$	–
		$\delta_{1b} = 15.0$	–
		$\delta_2 = 6.4$	$\theta_2 = 20^\circ$
		$\delta_3 = 7.2$	$\theta_3 = 90^\circ$
		$\delta_4 = 1.0$	–

Note: θ —cord angle in relation to the rolling direction. The indexes of the measures have the following meaning: $1a$ —tread part with a pattern, $1b$ —continuous tread part, 2—breaker, 3—cord, 4—inner sealing liner.

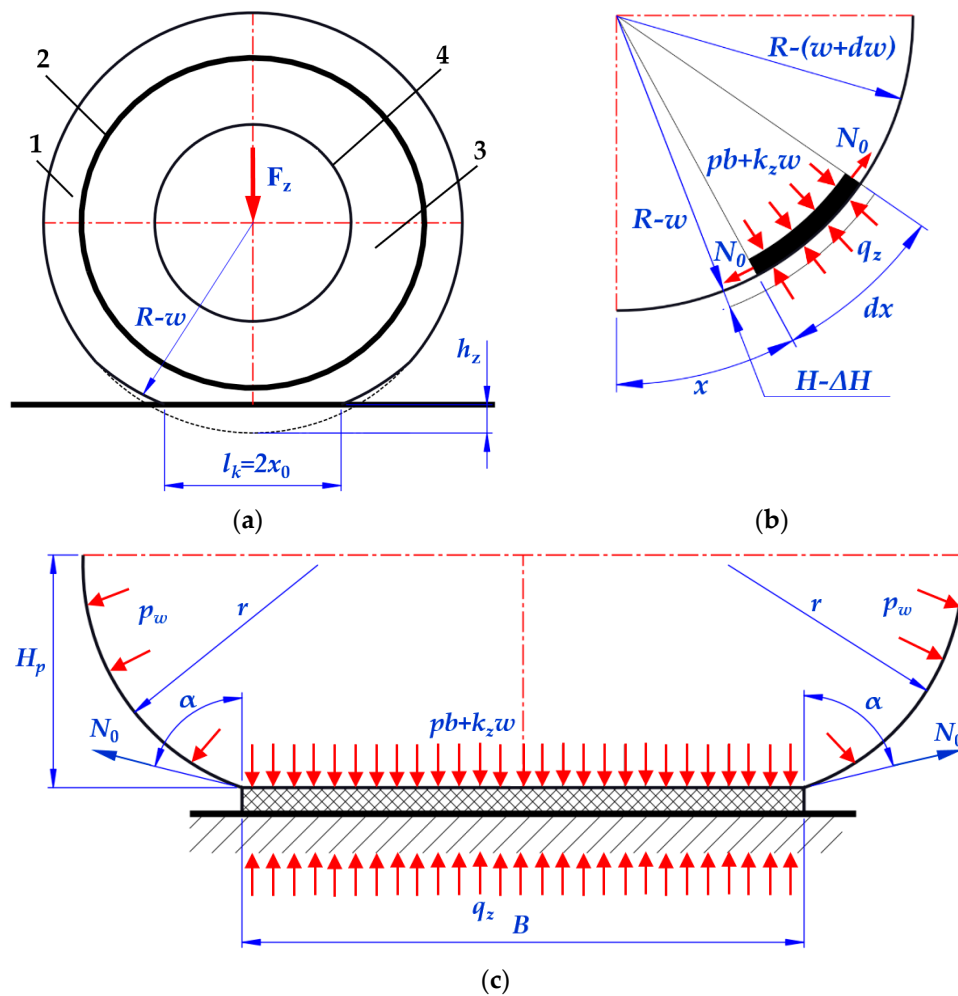


Figure 4. Model of the deformable ring of the tire: (a) deformable ring; (b) deformable ring element; (c) cross-section scheme for assessing the impact of the cord; 1—elastic layer (tread); 2—breaker layers; 3—elastic base (side walls); 4—disk.

Where the impact of the cord threads is assessed, the radial deformation model is used, and the tire reaction is assessed using single pressure $q_z = C_z w$. The sidewalls react only to the displacements in the radial direction, and the reaction per length unit equals $q_s = C_{zs} w$. An elastic outer layer with the thickness equal to H before deformation deforms by ΔH in the contact area. Inelastic forces are not subject to assessment. Tread reaction:

$$q_z = C_{zs} \Delta H 0 \tag{2}$$

Arc length x (Figure 4b) is measured from the center of contact. The main measures sought are [38]:

- model deflection h_z assuming that the band does not deform in the radial direction:

$$h_z = (w + \Delta H) \Big|_{x=0} \tag{3}$$

- contact zone length— $2x_0$;
- contact pressure distribution— $q_z(x)$;
- load F_z :

$$F_z = 2 \int_0^{x_0} q_z(x) dx \tag{4}$$

As a result of integration and rearrangement of Equation (4), the following is obtained:

$$F_z = 2k_{zs}x_0 \left[a_0 \left(1 - \frac{th\alpha x_0}{\alpha x_0} \right) - a_1 x_0^2 \left(\frac{1}{3} - \frac{th\alpha x_0}{\alpha x_0} \right) \right] \quad (5)$$

The unknown measures h_z and x_0 are determined using the following dependencies [38]:

$$h_z = \frac{x_0^2}{2R} \left(1 + m \frac{2}{\beta x_0} \right), \beta = \sqrt{k_z/N_0}, m = \left(1 - \frac{\beta^2}{\alpha^2} \right) \frac{1 - (th\alpha x_0/\alpha x_0)}{1 + (\beta/a)th\alpha x_0} \quad (6)$$

The described methodology validates the specifics of the tire ring load, namely, that the tire pressure in the contact area is not equal to the internal pressure of the tire due to the breaker and the cord layers. In order to refine the model, the deformation characteristics of the ring consisting of the cord and breaker layers and the tread as a separate deformable element are determined.

2.2. Deformation Properties of the Ring

In order to determine the deformation characteristics of the tire, the tire is divided into elements in the band consisting of the tread, breaker, cord, and protective layers attached by a flexible joint to the sides by the cord-reinforced rubber. The deformation characteristics of the individual tire elements were determined by breaking them down into monolayers made of rubber or rubber reinforced with unidirectional fiber. The elastic characteristics of the monolayer were determined according to the composite mechanic's equations [39–42]:

$$E_{C1} = E_f \phi_f + E_m (1 - \phi_f), E_{C2} = E_m \left((1 - \phi_f) + \frac{E_m}{E_{f2}} \phi_f \right)^{-1} \quad (7)$$

$$G_{C12} = G_m \left((1 - \phi_f) + \frac{G_m}{G_{f12}} \phi_f \right)^{-1}, \nu_{C12} = \phi_f \nu_{f12} + \phi_m \nu_m \quad (8)$$

where E_c and G_c —modulus of elasticity and shear of the composite; E_m and G_m —modulus of elasticity and shear of the matrix; E_f and G_f —the modulus of elasticity and shear of the filler; ϕ_f and ϕ_m —volumetric parts of the filler and matrix; ν_c , ν_f , and ν_m —Poisson's coefficients of the composite, filler and matrix; indices 1, 2—the direction along the fiber and the direction transverse to the fiber, respectively.

The properties of the cord and breaker layers in the longitudinal and transverse directions were determined using expressions of the plane stress state for the anisotropic monolayer [39–42]:

$$\begin{Bmatrix} \varepsilon_x \\ \varepsilon_y \\ \gamma_{xy} \end{Bmatrix} = \begin{Bmatrix} \frac{1}{E_x} & -\frac{\nu_{yx}}{E_y} & \frac{\eta_{xy}}{G_{xy}} \\ -\frac{\nu}{E_x} & \frac{1}{E_y} & \frac{\mu_{xy}}{G_{xy}} \\ \frac{\eta_x}{E_x} & \frac{\mu_y}{E_y} & \frac{1}{G_{xy}} \end{Bmatrix} \begin{Bmatrix} \sigma_x \\ \sigma_y \\ \tau_{xy} \end{Bmatrix} \quad (9)$$

The components of the elasticity matrix were determined according to [39–42] using the axes provided in Figure 5:

$$\begin{aligned}
E_x(\theta) &= \left(\frac{c^4}{E_1} + \frac{s^4}{E_2} + c^2s^2 \left(\frac{1}{G_{12}} - 2\frac{\nu_{21}}{E_2} \right) \right)^{-1}, \\
E_y(\theta) &= \left(\frac{s^4}{E_1} + \frac{c^4}{E_2} + c^2s^2 \left(\frac{1}{G_{12}} - 2\frac{\nu_{21}}{E_2} \right) \right)^{-1}, \\
G_{xy}(\theta) &= \left(4c^2s^2 \left(\frac{1}{E_1} + \frac{1}{E_2} + 2\frac{\nu_{21}}{E_2} \right) + \frac{(c^2-s^2)^2}{G_{12}} \right)^{-1}, \\
\frac{\nu_{yx}}{E_y}(\theta) &= \frac{\nu_{21}}{E_2} (c^4 - s^4) - c^2s^2 \left(\frac{1}{E_1} + \frac{1}{E_2} - \frac{1}{G_{12}} \right), \\
\frac{\eta_{xy}}{G_{xy}}(\theta) &= 2cs \left\{ \frac{s^2}{E_2} + \frac{c^2}{E_1} - (c^2 - s^2) \left(\frac{\nu_{21}}{E_2} - \frac{1}{2G_{12}} \right) \right\}, \\
\frac{\mu_{xy}}{G_{xy}}(\theta) &= 2cs \left\{ \frac{c^2}{E_2} + \frac{s^2}{E_1} + (c^2 - s^2) \left(\frac{\nu_{21}}{E_2} - \frac{1}{2G_{12}} \right) \right\}, \\
\eta_x &= \frac{\eta_{xy} E_x}{G_{xy}}, \quad \mu_y = \frac{\mu_{xy} E_y}{G_{xy}}
\end{aligned} \tag{10}$$

where $c = \cos\theta$ and $s = \sin\theta$; x -direction forming an angle θ with the reinforcement direction (Figure 5).

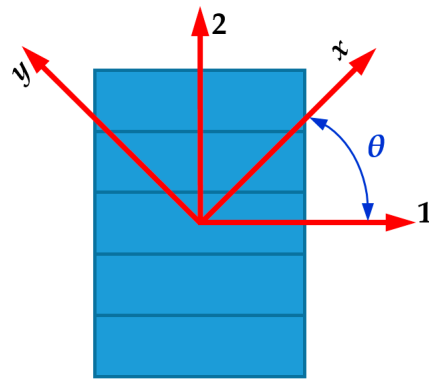


Figure 5. Layered composite element: 1-the direction along the fiber; 2-the direction transverse to the fiber.

The modulus of elasticity of the components and the Poisson's coefficients were taken from the works [36,43]. The methodology used for this purpose is presented in [39–42]. Direct modulus of elasticity calculations does not provide an answer in relation to the characteristics of the tread and unreinforced ring section that are required for the model provided in Figure 4. To determine the stiffness of the tread C_z , tread deformations are analyzed additionally. The obtained data are presented in Table 2.

2.3. Investigation of Tread Deformation

Tread deformations were investigated using several models: porous composite and rubber prism models. The research studies analyzing the pneumatic tires specify fairly wide limits of the modulus of elasticity of rubber $E_r = 2 \dots 20$ MPa. In the study [36], a simplified model of a passenger car tire was used, $E_r = 18$ MPa, in order to obtain adequate deformation characteristics of the whole tire. In order to specify the initial characteristics, an experiment was performed to determine the 313 mm wide section of the tread band of the truck tire corresponding to 12.00R20 tire treads. The height of the tread part with a pattern was $\delta_{1a} = 17.8$ mm, without pattern $\delta_{1b} = 3.9$ mm. At compression, the tread was under the action of the load corresponding to the nominal radial load R_{znom} of the 12.00R20 type tires in terms of the pressure. An experimental setup for monotonous tension compression tests consisted of a 50 kN testing machine Instron (Norwood, MA, USA) 8801 series and an electronic device that was designed to record the stress-strain curves. The mechanical characteristics were measured with an error not exceeding $\pm 1\%$ of the deformation scale. The data collection was performed by using the Bluehill Universal Software. Compression tests were performed in accordance with ASTM D575-91: Standard Test Methods for Rubber Properties in Compression.

The obtained load-deformation dependence (Figure 6) is very close to the linear (correlation coefficient $r_{xy} = 0.947$), proving the applicability of the description of the linear elastic material to the study of tread deformations. The obtained modulus of tread elasticity

determined on the basis of the experimental results was 7.84 MPa, taking into consideration the tread part with a pattern according to the filling factor, $E_r = 6.16$ MPa, which was much lower than in the study [36].

Table 2. Modulus of elasticity of the tire elements, MPa.

Characteristics	Tire				
	A	B	C	D	
Breaker (with nylon)	E_l	$1667 \cdot 10^3$	$1667 \cdot 10^3$	—	$1367 \cdot 10^3$
	E_t	26,736	26,736	—	24,568
	E_r	26,736	26,736	—	24,568
Breaker (with steel)	E_l	73,119	73,119	73,119	73,119
	E_t	21,737	21,737	21,737	21,737
	E_r	23,684	23,684	23,684	23,684
Cord (with viscose)	E_l	24,625	24,625	26,819	—
	E_t	$3553 \cdot 10^3$	$3553 \cdot 10^3$	$4339 \cdot 10^3$	—
	E_r	24,625	24,625	26,819	—
Inner sealing layer E	18	18	18	18	
Part of the ring up to the cord E	16,601	16,630	17,118	16,511	
Whole ring E	16,890	16,906	17,311	16,541	
Sidewall elasticity modulus during radial tension E_r	507.5	531.15	788.1	551.7	
Equivalent sidewall elasticity modulus during radial bending E flat band,	ring.	23.32	24.37	29.77	67.89
	ring.	42.69	43.04	61.51	113.4
Equivalent modulus of elasticity of the band bending E_c flat band in the circular direction, perpendicular to the circular direction ring, in the circular direction.		15.89	17.74	19.63	15.92
		15.35	17.37	16.34	15.90
		23.73	24.21	22.50	18.50
Relative position of the neutral layer $e / \sum \delta$ at bending flat band in the circular direction, perpendicular to the circular direction ring, in the circular direction.		0.288	0.281	0.383	0.377
		0.108	0.11	0.088	0.124
		0.286	0.277	0.376	0.372

Note: E —in all directions, E_l —the rolling direction of the tire, E_t —perpendicular to the rolling direction of the tire, and E_r —in the radial direction (in relation to the tire).

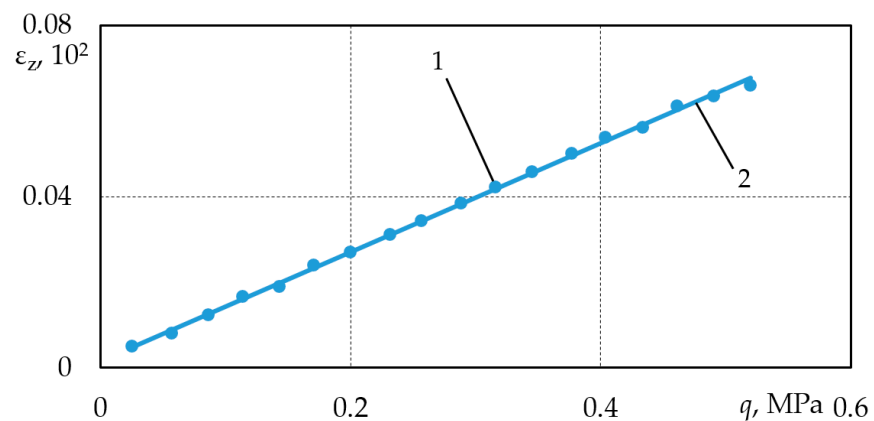


Figure 6. Summary experimental data: 1—experimental data; 2—generalized line.

Whereas the tread consists of the parts with and without a pattern and the deformation properties of the tread are evaluated in the model as a single generalized layer, the possibilities of assessment of the tread part with a pattern were examined. The simplest model assesses the filling of the part with a pattern (Figure 7), which can be executed using the expression of porous composites [44]:

$$E = k_u E_g \tag{11}$$

where k_u —tread filling factor, where $k_u = A_i/A_p$, A_i —the area of the continuous pattern in the part of the tread part selected according to the repetition of the pattern, A_p —area of the selected part of the tread; and E_g —tread rubber modulus of elasticity.

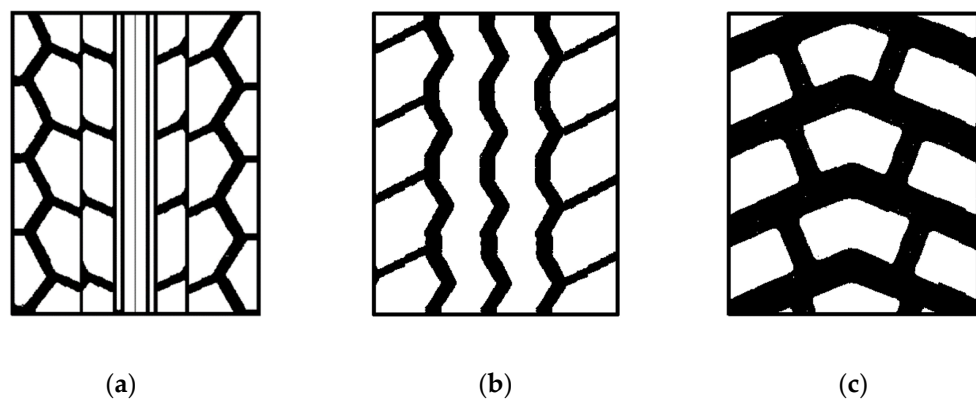


Figure 7. Tire tread patterns: (a) for a passenger car; (b) for a light-duty truck; and (c) for a truck.

Since the tread pattern is different across differed parts of the tread (Figure 7), the filling factor for each tread band was calculated separately. In this case, the equivalent modulus of elasticity of the tread was equal to:

$$E_1 = E_g \frac{\sum k_{ui} k_{bi}}{1 - k_a (1 - \sum k_{ui} k_{bi})} \tag{12}$$

where E_g —tread rubber modulus of elasticity; $k_a = \delta_{1a}/\delta_1$; $\delta_1 = \delta_{1a} + \delta_{1b}$; k_{bi} —share of the width of the i -th band in the width of the tread, δ_1 —tire tread thickness, δ_{1a} —tread part with a pattern, and δ_{1b} —continuous part of the tread.

The results obtained for different tires are presented in Table 3. The modulus of elasticity of the whole tread was calculated using the equation in [44]:

$$\frac{1}{E_1} = \left(\frac{\delta_{1a}}{E_{1a}} + \frac{\delta_{1b}}{E_{1b}} \right) \cdot \frac{1}{\delta_1} \tag{13}$$

Table 3. Tread modulus of elasticity obtained by assessment using the first model, MPa.

Tire Type	Part with a Pattern E_{1a} ,	Continuous Part E_{1b} ,	Tread E_1 ,
A	5.72	7.84	6.16
B	5.88	7.84	6.22
C	7.08	7.84	6.51
D	5.33	7.84	5.37

This model does not accurately reflect the operating conditions of the tread. Deformation of the tread part with a pattern may be restricted by the contact with the road or a continuous breaker. Moreover, the deformation of the tread part with a pattern does not fully correspond to the ideal compression conditions, as the deformation of the ends at

compression leads to a change in the element shape. The course of deformation would be more accurately estimated using the model of a prism subject for compression by applying a rubber-shock-absorber calculation methodology.

The deformations of the tread part with a pattern can be assessed more precisely using the calculation methods applicable to the rubber shock absorbers. Under this approach, the tread element is depicted as a rubber prism, deformed with more or less constrained end deformations depending on the conditions. If the deformations of the both ends of the prism-shaped rubber shock absorber are constrained, the relationship between the load and the deformation is expressed by the equation:

$$R_z = \frac{1}{3}\beta EA \left(\frac{1}{\lambda^2} - \lambda \right), \lambda = 1 - \frac{\Delta\delta}{\delta}, \beta = \frac{4}{3} \left(1 + \eta^2 - \eta \right) \left(1 - \frac{2}{\alpha\delta} th \frac{\alpha\delta}{2} \right)^{-1} \tag{14}$$

where A —prism base area; δ —prism height; $\Delta\delta$ —prism deformation; and α and η —shape change parameters. Whereas α and η are interrelated, a system of equations derived from the energy minimum condition is proposed in the study [45]:

$$\alpha^2 = \frac{1}{b^2} \frac{48(1+\eta^2-\eta)}{\eta^2(\frac{a}{b})+(1-\eta)^2}, \tag{15}$$

$$\frac{\alpha\delta - 2th \frac{\alpha\delta}{2}}{\alpha\delta(th^2 \frac{\alpha\delta}{2} - 1) + 2th \frac{\alpha\delta}{2}} = \frac{1}{2} + \frac{1+\eta^2-\eta}{1-2\eta} \frac{\eta(\frac{a}{b})^2 + \eta - 1}{\eta^2(\frac{a}{b})^2 + (1-\eta)^2}$$

where a, b —dimensions of the prism base.

Equations (14) and (15) were solved by approximation.

This model of the tread part with a pattern was applied to two cases: with the end deformations not constrained and with the end deformations completely constrained. If the deformations of the shock absorber ends were not constrained, $\beta = 1$. In case the deformations were constrained, the stiffness of the individual bands of the tread part with a pattern would increase by up to 4.5 times (Table 4).

Table 4. The values of the stiffening coefficient of the tread elements for individual tread bands.

Tire Type	Band Number	Length a , mm	Width b , mm	β Band
A	1	39	29	3.83
	2	32	29.6	3.67
B	1	37	29	3.75
	2	31	29	3.67
	3	239	24	4.58
C	1	33	20	2.62
	2	36	18	2.08
D	1	116	42	3.33
	2	90	41	3.17

Under actual conditions, the constraints of the end deformations of the tread part with a pattern were not absolute. In relation to the contact with the road, they are determined by the tire-road friction, while the other end is in contact with the tread part without a pattern. Deformations of the tread part without a pattern are restricted by the breaker layers that have the anisotropic properties (Table 2), and the modulus of elasticity of the layer is only 1.2–1.5 times higher than the modulus of elasticity of rubber in the direction transverse to the reinforcement. Under these conditions, the deformation conditions of the tread part with a pattern are closer to those of a shock absorber with freely deforming ends. This option was used for further calculations.

Both models offer different characteristics: the modulus of elasticity E_1 or deformation $\Delta\delta$ corresponding to the radial load R_z value. For comparison of the results, the generalized characteristic describing the relationship between load and deformation—stiffness C_1 was used:

$$\Delta\delta = C_1 \cdot R_z \quad (16)$$

where C_1 —tread stiffness and R_z —radial load of the tire.

When determining the measure C_1 according to the first or second models, it should be taken into the account that the road contact area and the volume of the deformable tread part depend on the load. The following assumptions were used when determining the area of the contact with the road:

- the contact with the road has an elliptical shape and is limited by the tire width and length of the contact with the road;
- the layers under the tread are sufficiently stiff, and their length does not change during deformation of the tire;
- there is the linear dependency between the radial deformation and radial load;
- the pressure is distributed evenly across the contact surface.

The provided assumptions enable determination of the pressure in the contact area. Nonlinear $q(R_z)$ dependence was obtained for all the tested tires (Figure 8). The tire load is calculated using the nominal load of the tire R_{znom} , which is specified in the catalogs, by setting the limits $R_{zmin} = 0.2R_{znom}$ and $R_{zmax} = 1.4R_{znom}$. The both models were compared to the first model by calculating the following:

$$\Delta\delta = q \cdot \delta / E_1 \quad (17)$$

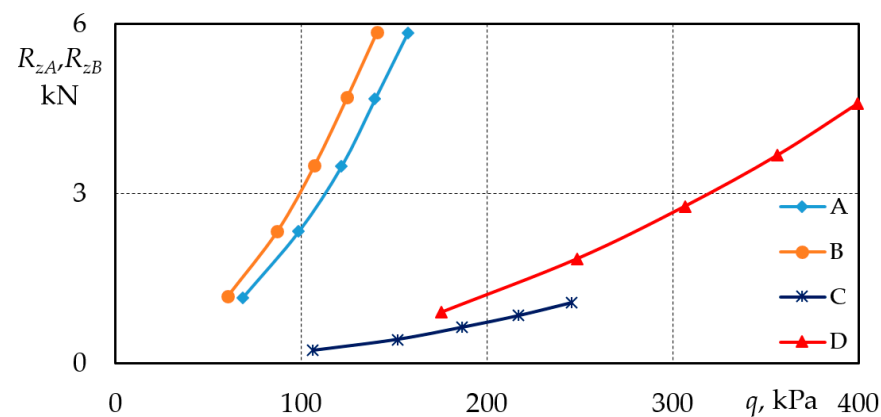


Figure 8. Radial loads of the tires (marking according to Table 2).

Nonlinear dependence was observed $C_{1a}(R_z)$ and was related to nonlinear dependence between R_z and the length of the contact with the road. This generated the nonlinear $q(R_z)$ dependence that reduced tread deformation in the area of higher loads. The specifics of the tire-road contact are explained by the fact that the type of tire $C_{1a}(R_z)$ has no significant effect on the nature of the dependence (Figure 9).

The influence of tread wear on its stiffness was determined using the second model that provides more accurate reflection of the deformation conditions of short rubber prisms [36]. The effect of prism end constraint was not assessed when calculating tread stiffness. For the calculation of the tread stiffness of type A tire, the tread height was 8.1 mm for a new tire and 1.6 mm for a worn tire, and an intermediate wear level (4.9 mm) was provided. The tread wear changed the $C-R_z$ dependence slightly (Figure 10) but had a significant effect on the stiffness value. The effect was not monotonic as the stiffness would be subject to particular change at the beginning of the wear. For the tested tires, tread wear could increase the stiffness of the tread in relation to the nominal load by up to 1.3 times.

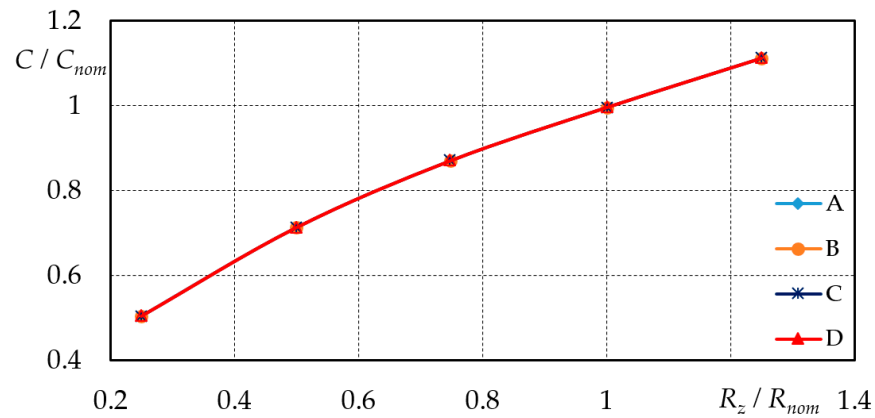


Figure 9. Dependence of relative stiffness of the tread part with a pattern on the relative radial load for different tires (compressed prism model; marking according to Table 2).

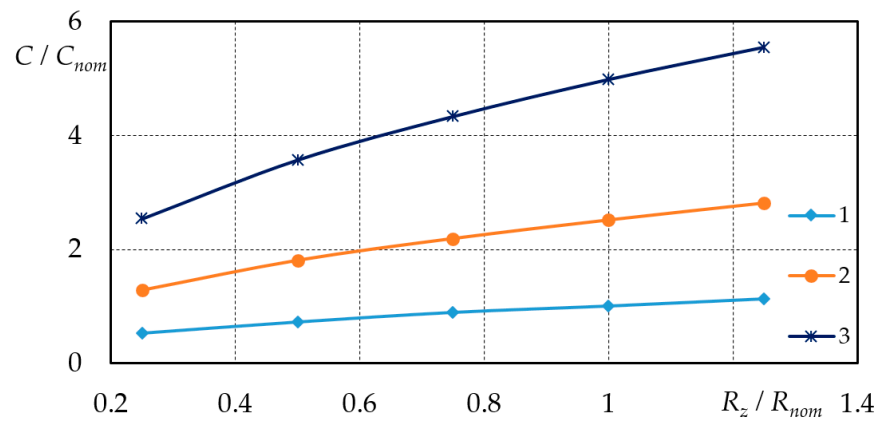


Figure 10. Dependence of stiffness of B tire tread part with a pattern on the tread height: 1—new tire; 2—worn by 50%; and 3—worn out.

Depending on the constraint conditions, the second model provided very different results. For more accurate assessment, the effect of the latter constraint, given that the properties of the ring consisting of the cord and breaker are anisotropic, and the influence of deformation characteristics of the tire ring consisting of the tread, breaker, cord and protective layer, on the tread properties were determined, and the road-to-tread contact model was adjusted.

The tape for Nokian passenger car tires 175/70R13 82T was modeled. Its more detailed structure is provided in Table 5.

Table 5. Layer distribution of 175/70R13 82T tire bands.

Layer No.	Layer Designation	Thickness, mm
1	Tread with a pattern	2.9
2	Tread without a pattern	2.1
3	Nylon-rubber	0.8
4	Steel-rubber	0.9
5	Rubber	0.9
6	Steel-rubber	0.9
7	Viscose-rubber	0.9
8	Sealing layer	0.9

The properties of the cord and breaker layers in the longitudinal and transverse directions were determined using expressions of the plane stress state for the anisotropic monolayer [39–42] by applying them to the axes presented in Figure 5:

$$\begin{aligned} \begin{Bmatrix} \varepsilon_x \\ \varepsilon_y \\ \gamma_{xy} \end{Bmatrix} &= [T'] \begin{Bmatrix} \frac{1}{E_1} & -\frac{\nu_{21}}{E_2} & 0 \\ -\frac{\nu_{21}}{E_2} & \frac{1}{E_2} & 0 \\ 0 & 0 & \frac{1}{G_{12}} \end{Bmatrix} [T] \begin{Bmatrix} \sigma_x \\ \sigma_y \\ \tau_{xy} \end{Bmatrix} \\ [T'] &= \begin{bmatrix} c^2 & s^2 & cs \\ s^2 & c^2 & -cs \\ -2cs & 2cs & (c^2 - s^2) \end{bmatrix}, [T] = \begin{bmatrix} s^2 & c^2 & -2sc \\ c^2 & s^2 & 2sc \\ sc & -sc & (c^2 - s^2) \end{bmatrix} \end{aligned} \quad (18)$$

where $c = \cos\theta$ and $s = \sin\theta$.

Deformation properties of the layers were determined according to the methodology set out in Section 2.2. An assumption was made that nylon and viscose fibers were anisotropic, with a different modulus of longitudinal elasticity and transverse to the fiber.

The issue of identification of the layers emerged in the investigation of the structure of the modeled tire band. There is a rubber layer between the individual bands of the breaker reinforced with steel wire. As a result, the band was investigated additionally by identifying the rubber layer between the reinforced layers (Figure 11a; Table 5) and using simplified separation into two layers (Figure 11b).

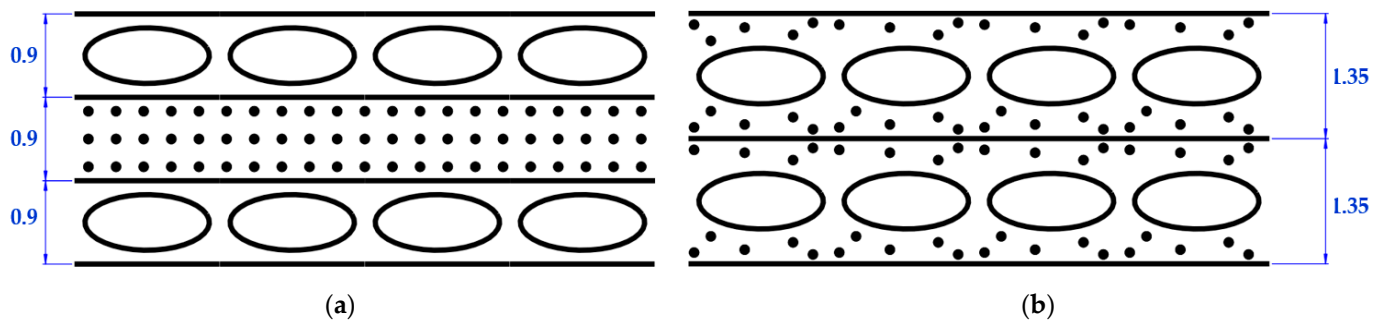


Figure 11. Breaker layer calculation schemes: (a) by identifying the intermediate rubber layer and (b) without identifying the intermediate rubber layer.

In the investigation of the deformation properties of the whole band, the model used in layered composites was applied initially. The calculated modulus of elasticity of the band as a composite was calculated by taking into consideration the modulus of elasticity of the layers joined in parallel (X and Y directions) or consistently (Z direction).

Since the reinforcement angles of the adjacent breaker layers differed by the sign only ($+20^\circ$ and -20°), it was assumed that the resulting shear forces in the layers were counterbalanced and were not transmitted to other layers.

Considering the large difference between the modulus of elasticity of the reinforcing fiber and the rubber, it was determined that the modulus of elasticity of the layer in the direction of reinforcement was not significantly affected by the modulus of elasticity of the rubber. The method of identification of the layers (a and b) also did not have any effect in this case. At the same time, it was found that the model of elasticity of the layer would be more dependent on the modulus of elasticity of the rubber in the breaker fiber direction X and Z . The modulus of elasticity in X direction was less dependent on the total modulus of elasticity E . By changing the modulus of elasticity of the rubber in the range of 2 . . . 20 MPa, E_x differed by 3.7% for model (a) and 3.5% for model (b). E_z dependence was particularly evident: rubber stiffness E_r would change 10 times, while E_z would change 9.97 times (Figure 12). Considering that the deformation properties of the band in Z direction differed considerably from the data provided by other authors, the assumption was that stiffer cord and breaker layers may restrict tread deformations, and in the state of constrained

deformation, tread deformation could be significantly influenced by the Poisson’s ratio close to 0.5. Therefore, tread deformation under compression was investigated additionally under the assumptions that reflected the interaction between the individual layers in the identified tire band more accurately.

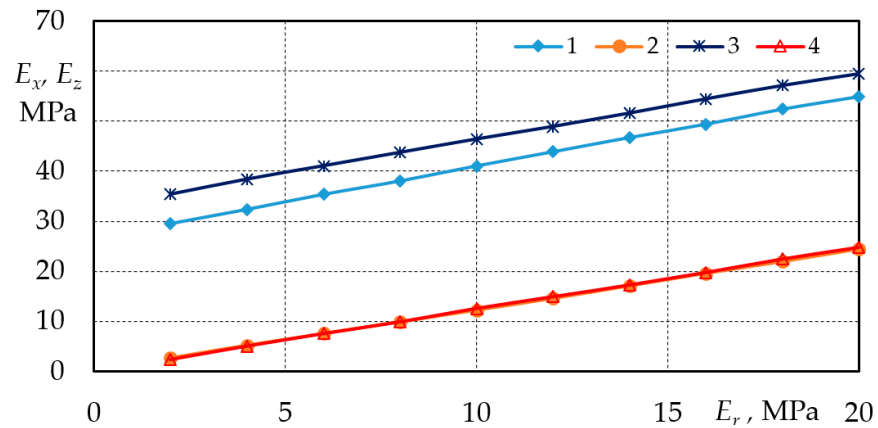


Figure 12. Tire band elastic modulus in X and Z directions: 1—model a (8 layers) in X direction, 2—model a in Z direction, 3—model b (7 layers) in X direction, and 4—model b in Z direction.

Two cases were examined for this purpose. In the first case, it was assumed that by deforming the band in Z direction, deformation of all layers was the same in X and Y directions:

$$\epsilon_{x1} = \epsilon_{x2} = \dots = \epsilon_{xn}, \epsilon_{y1} = \epsilon_{y2} = \dots = \epsilon_{yn} \tag{19}$$

The sum of the resulting single axial forces in the individual layers in the X and Y axis directions equaled zero:

$$\begin{aligned} \delta_1\sigma_{x1} + \delta_{x2}\sigma_{x2} + \dots + \delta_n\sigma_{xn} &= 0, \\ \delta_1\sigma_{y1} + \delta_{y2}\sigma_{y2} + \dots + \delta_n\sigma_{yn} &= 0, \\ \sigma_{z1} = \sigma_{z2} = \dots = \sigma_{zn} &= \sigma_z = q. \end{aligned} \tag{20}$$

The numerical experiment showed that the modulus of elasticity of rubber in Z direction would increase greatly and result in an increase in the modulus of elasticity of the entire band in Z direction (Figure 13).

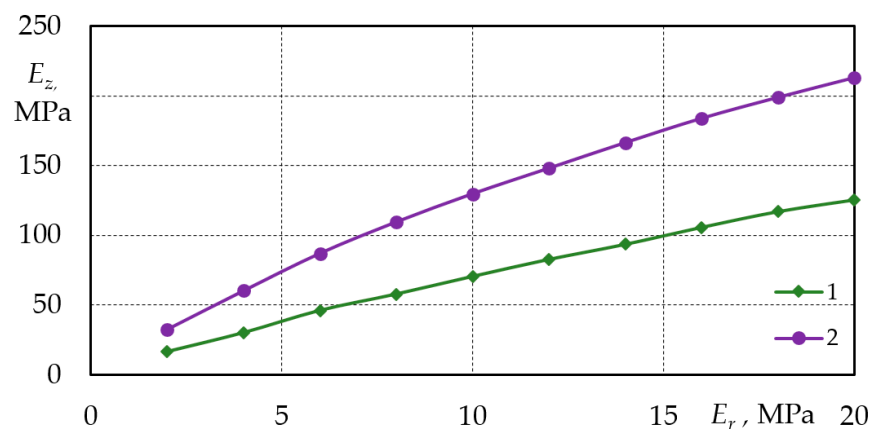


Figure 13. Dependence of the tire band modulus of elasticity on the modulus of elasticity of rubber ($\sigma_z = 0.2$ MPa): 1–7 layers and 2–8 layers.

The numerical experiment confirmed that the models predicting uniform layer deformation were particularly sensitive to components with the Poisson’s ratio close to 0.5. The conditional modulus of elasticity of the rubber with the layer structure corresponding to the 175/70R1382T tire, depending on the layer, was 86.3 MPa. For this reason, the model with the identified intermediate layer of rubber predicted an unrealistically high stiffness.

In the second case, the tread-to-road friction was assessed, and an assumption was made that the tread deformation would be constrained as long as the shear force developing in directions *X* and *Y* did not exceed the frictional force. Whereas the control experiment was anticipated, the numerical model assumed that the frictional forces would also act on the other side of the band, i.e., in contact with the sealing liner. The constraint provided that the stresses in *X* and *Y* directions could not exceed the limit values:

$$\sigma_{xr} = \sigma_{yr} = \mu\sigma_z \tag{21}$$

where μ —coefficient of friction between rubber and steel.

The numerical experiment confirmed that friction had an impact on the E_z measure (Figure 14). As the coefficient of friction increased, the stiffness of the band in the transverse direction would increase rapidly. The identified additional rubber layers had a smaller influence in this case (Figure 14).

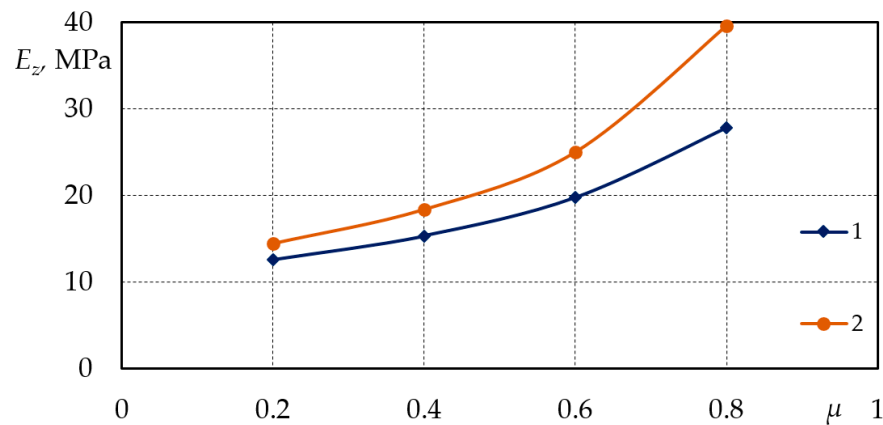


Figure 14. Dependence of tire band deformation on the coefficient of friction ($\sigma_z = 0.2$ MPa, $E_r = 6$ MPa) using different breaker models: 1—7 layers and 2—8 layers.

To revise the results obtained, it was attempted to deform the band cut from the tire in the *Z* direction. The experiment was performed using the 175/70R1382T Nokian tire band used for modeling. The summarized experimental data are presented in Figure 15.

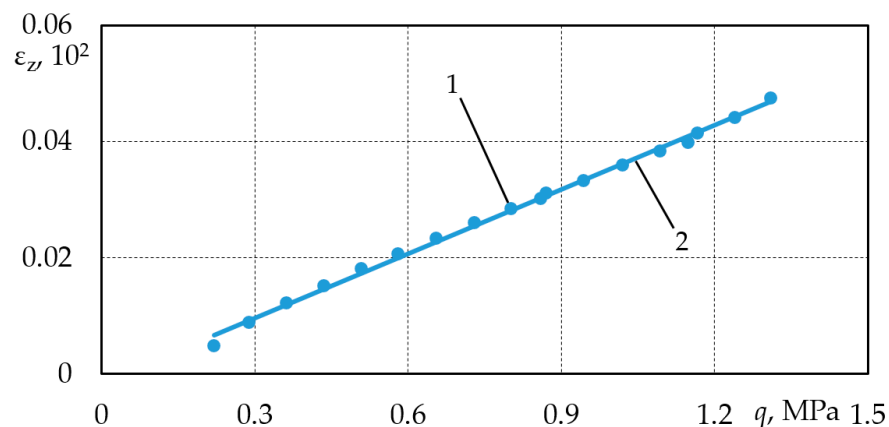


Figure 15. Summary experimental data: 1—experimental data and 2—generalized line.

The experiment confirmed that the linear relationship between pressure and deformation remained up to the pressures above the operating pressure range (tested up to $q = 1.5$ MPa). The calculated modulus of elasticity of the whole band was 27 MPa, which corresponded to the numerical model of the simplified model structure (7 layers) assessing the friction between the plates and the band.

In the simplified tire models, the cord was assessed during the calculation of radial loads. Therefore, the breaker layers could also be considered as conditionally involved in the radial deformation of the tread. Thereby, the calculation expressions of the layered composites with sequentially arranged layers would result in the following:

$$\frac{1}{C_{prz}^*} = \frac{\delta_1}{C_{1z}^*} + \frac{\delta_2}{C_{2z}^*} + \frac{\delta_3}{C_{3z}^*} \quad (22)$$

where C_i^* —member of the stiffness matrix accounting for the deformation constraint.

If the stiffness of the band used in the experiment was modeled with a layered composite with sequentially arranged layers, its stiffness could be estimated by Equation (22). In this case, the member of the stiffness matrix of the tested tire tread E_z^* would be equal to 27 MPa. This value was used in the research for determination of the C_z measure in Equation (22).

For real tread modeling, tread loads and operating conditions need to be adjusted by bringing the numerical model closer to real conditions. The third tread deformation model was used to evaluate the specifics of the tire-road texture interaction. Road texture means unevenness of the road pavement. For asphalt pavement, the height of the unevenness was 1–5 mm. The irregularities were assumed to be hemispherical protrusions of regular spacing (Figure 16). This assumption enabled modeling of the interaction of an individual unevenness with the tread, assuming that the unevenness acted on the continuous part of the tread. The coefficient of filling with spheres necessary for the conversion of the reference pressure was equal to $\pi/4 = 0.785$. Based on the geometrical conditions, it was determined that the gaps between the spheres would be filled at the sphere penetration into the tread equal to: $\Delta = 0.455r$, where r —radius of the sphere. The known spheres used for the investigation of interaction were the solution for the elastic deformations of the plane contact. The interaction scheme is shown in Figure 17.

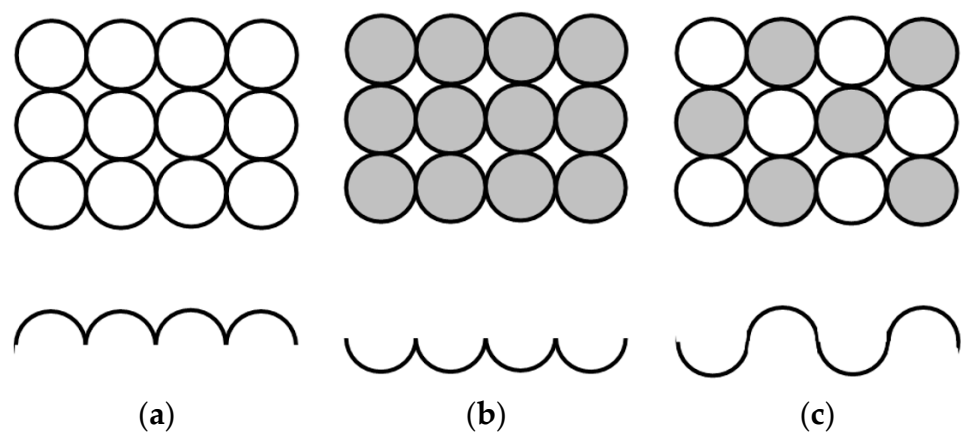


Figure 16. Road unevenness schemes: (a)—convexities; (b)—concavities; (c)—combination of convexities and concavities.

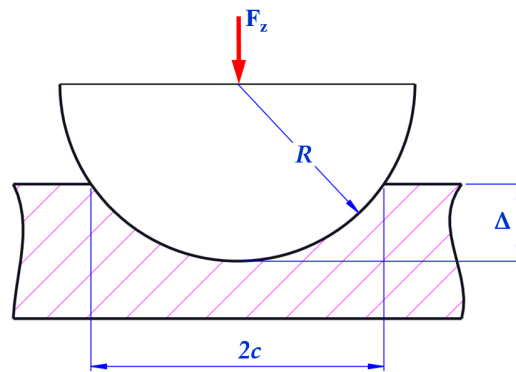


Figure 17. Unevenness-to-tread interaction scheme.

The hemisphere-shaped unevenness with radius r pressed against the tread located on a rigid base with force F . As a result, the unevenness penetrated into the tread to depth Δ . The radius of the depression was equal to c . The elastic solution for the task was known and taken from [45]. The depression radius c was equal to:

$$c = 0.721 \cdot \sqrt[3]{2 \cdot F \cdot r \cdot (k_1 + k_2)} \tag{23}$$

where $k_i = 1 - \nu_i^2 / E_i$; E_i, ν_i —the modulus of elasticity and Poisson’s ratio of the spherical and planar material ($E_1 = 18 \text{ MPa}, \nu_1 = 0.5, E_2 = 6 \text{ MPa}, \nu_1 = 0.3$) [36].

Average contact pressure:

$$q_0 = 0.918 \cdot \sqrt[3]{F / (2 \cdot r \cdot (k_1 + k_2))^2} \tag{24}$$

F measure was to make sure that pressure q acting at the tire-road when the tire was subjected to force R_z would be equal to the mean pressure at the sphere-to-tread contact q_0 , taking into account the coefficient of filling with spheres at the contact. Considering that, according to the elastic solution:

$$\Delta = 0.8255 \cdot \sqrt[3]{\frac{F^2}{r} (k_1 + k_2)^2}, \quad q_0 = \frac{F}{\pi \cdot c^2} \tag{25}$$

and after introduction of the condition $q_0 = q$, the result would be:

$$\Delta = 5.552q^2r(k_1 + k_2)^2 \tag{26}$$

The tread stiffness values obtained for the individual models are presented in Figure 18.

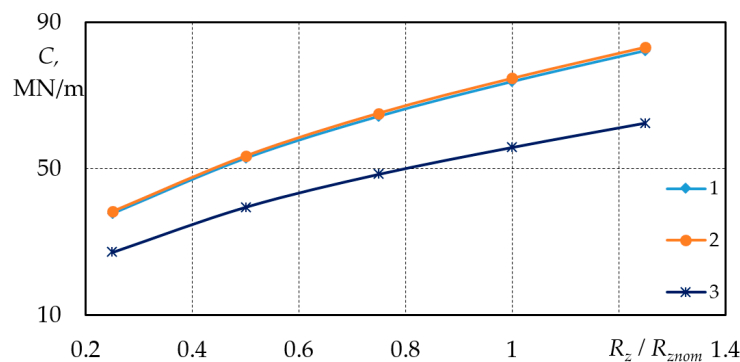


Figure 18. Dependence of the stiffness of the patterned part of tire 175/70R13 on the relative radial load using different models: 1—porous composite model, 2—compressible prism model, and 3—road-tire contact model.

The calculations confirmed that in the case of 5 mm high unevenness, condition $\Delta < 0.455r$ (the tread does not fill the entire volume between the unevennesses) would be met for the pressures at the tire-road contact. This result demonstrates that the gaps between the road unevenness elements of this shape and size are not completely filled by the tread and enable better adhesion to the road and removal of moisture from the tire-road contact area. Road texture interaction model ($r = 5$ mm) indicates lower stiffness values; however, dependence CR_z remains similar and is related to nonlinear qR_z dependence. In addition, it was confirmed that a simplified model estimating the modulus of elasticity of the tread band could be used for the assessment of the tread deformation. The modulus of elasticity of the tread material should be determined by assessing the deformation constraint.

3. Vehicle Excitation by Road Unevenness

Vehicle stability was assessed using several criteria. One of them was the stability of the linear motion of the steered wheels measured at a critical speed, above which the wheels started to vibrate about the vertical axis. The cause of the vibrations was the suspension vibrations. Therefore, the issue of car stability would be analyzed starting with the formation of the differential equations for a system consisting of a steering wheel mechanism, suspension, and wheels. At the initial moment, the number of elements comprising the system was reduced, i.e., the body vibrations were not taken into account. Body vibrations were not evaluated because its free vibration frequency was significantly lower than the suspension and wheel vibration frequency.

3.1. Suspension Models

When considering road excitation, it was necessary to specify which of the car's vertical motion models best met the requirements for stability models. Three vertical dynamics models are known: (1) quarter-car, (2) flat (2D), and (3) spatial (3D), examined in the studies [46–57]. The 2D model best describes the longitudinal vehicle dynamics, i.e., braking, acceleration, vertical obstacle clearance, etc., and will not be used in future investigations.

The simplest model used for road-vehicle interaction analysis is the quarter-car model. It consists of three masses: tire element m_1 , unsprung masses (suspensions) m_2 , and sprung masses (body) m_3 (Figure 2). This model enables the calculation of the maximum and characteristic values of the vertical displacements of the wheel and to specify the frequency characteristic of the suspension. More accurate models were found to require a more accurate assessment of tire performance, such as damping. The dimensions of the tire tread element were determined according to Figure 3, while the length of the contact was according to Equation (1) expression. The tread stiffness coefficient was determined using Equation (2). Quarter-car model behavior under kinematic excitation by road unevenness q was described using the following system of equations:

$$\begin{aligned} m_1 \ddot{z}_1 + k_1(\dot{z}_1 - \dot{q}) + c_1(z_1 - q) &= 0, \\ m_2 \ddot{z}_2 + k_2(\dot{z}_2 - \dot{z}_1) + c_2(z_2 - z_1) &= 0, \\ m_3 \ddot{z}_3 + k_3(\dot{z}_3 - \dot{z}_2) + c_3(z_3 - z_2) &= 0. \end{aligned} \quad (27)$$

where m_1, m_2, m_3 —tread part of the tire, unsprung, and sprung mass, respectively; z_1, z_2, z_3 —tire, suspension and body displacements, respectively; k_1, k_2, k_3 —tread, tire, and suspension damping factors, respectively; c_1, c_2, c_3 —stiffness of the tread, tire, and suspension, respectively; and q —height of road profile unevenness.

When developing the 3D model of the car, the following assumptions were made: the car body would be symmetrical with respect to the longitudinal and transverse axes, and its center of gravity would be on the car symmetry plane. For the first approach, it was assumed that the masses of the wheels would move only in the vertical direction, with the track of the front and rear axes being the same. The vertical oscillations of the 3D car model on the longitudinal plane were calculated using the system of Equation (27).

The transverse tilt of the car was expressed by the system of equations:

$$[M_\beta] \cdot \{\ddot{\beta}\} + [K_\beta] \cdot \{\dot{\beta}\} + [C_\beta] \cdot \{\beta\} = [M_q] \quad (28)$$

where $\{\beta\}$ —transverse displacement vector consisting of $\beta_{1g} = \frac{1}{t_2}(z_{12k} - z_{11d})$, $\beta_{1p} = \frac{1}{t_2}(z_{11k} - z_{11d})$; indexes $1i$ —front, $2i$ —rear, k —left, d —right, t_1 —front track of the car, and t_2 —rear track of the car.

Mass matrix:

$$[M_\beta] = \begin{bmatrix} I_x & 0 & 0 \\ 0 & 2m_{11}\left(\frac{t_1}{2}\right)^2 & 0 \\ 0 & 0 & 2m_{12}\left(\frac{t_2}{2}\right)^2 \end{bmatrix} \quad (29)$$

where I_x —moment of inertia of the sprung mass of the vehicle around the longitudinal axis of the tilt and t —wheel track of the respective axis.

Damping matrix:

$$[K_\beta] = \begin{bmatrix} \frac{1}{2}(k_{21}t_1^2 + k_{22})\left(\frac{t}{2}\right)^2 & -\frac{k_{21}t^2}{2} & -\frac{k_{22}t^2}{2} \\ -\frac{k_{21}t^2}{2} & \frac{(k_{11}+k_{12})t_1^2}{2} & 0 \\ -\frac{k_{22}t^2}{2} & k_{11} + k_{21} & \frac{(k_{12}+k_{22})t_2^2}{2} \end{bmatrix} \quad (30)$$

Stiffness matrix:

$$[C_\beta] = \begin{bmatrix} \frac{1}{2}(c_{21}t_1^2 + c_{22})\left(\frac{t}{2}\right)^2 & -\frac{c_{21}t^2}{2} & -\frac{c_{22}t^2}{2} \\ -\frac{c_{21}t^2}{2} & \frac{(c_{11}+c_{12})t_1^2}{2} & 0 \\ -\frac{c_{22}t^2}{2} & c_{11} + c_{21} & \frac{(c_{12}+c_{22})t_2^2}{2} \end{bmatrix} \quad (31)$$

The pavement influence matrix must take into account that the excitation on the left and right sides may be unequal and was therefore expressed as:

$$[M_q] = \begin{bmatrix} 0 & 0 \\ 2c_{12}\left(\frac{t_1}{2}\right)^2 & 0 \\ 0 & 2c_{12}\left(\frac{t_2}{2}\right)^2 \end{bmatrix} \cdot \begin{Bmatrix} q_{\Delta 1} \\ q_{\Delta 2} \end{Bmatrix} \quad (32)$$

where $q_{\Delta 1} = \frac{1}{t_1}(q_{1k} - q_{2d})$, $q_{\Delta 2} = \frac{1}{t_2}(q_{2k} - q_{2d})$, with $q_{\Delta 1}$ - and $q_{\Delta 2}$ —angular differences in road unevenness at the front and rear axes of the vehicle, respectively.

The quarter-car and 3D car models (the characteristics of the model elements are presented in Table 6, and modeling results are presented in Figure 19) were compared numerically by modeling the compact car movement on a city-type road at the speed of 40 km/h and 80 km/h, taking into account the nonlinearity of the characteristics of the tire and the elastic members.

Figure 19 shows that in the case of the 3D model, larger vertical displacements of the sprung masses (up to 20%) were obtained, but the overall curve characteristic remained almost without any changes.

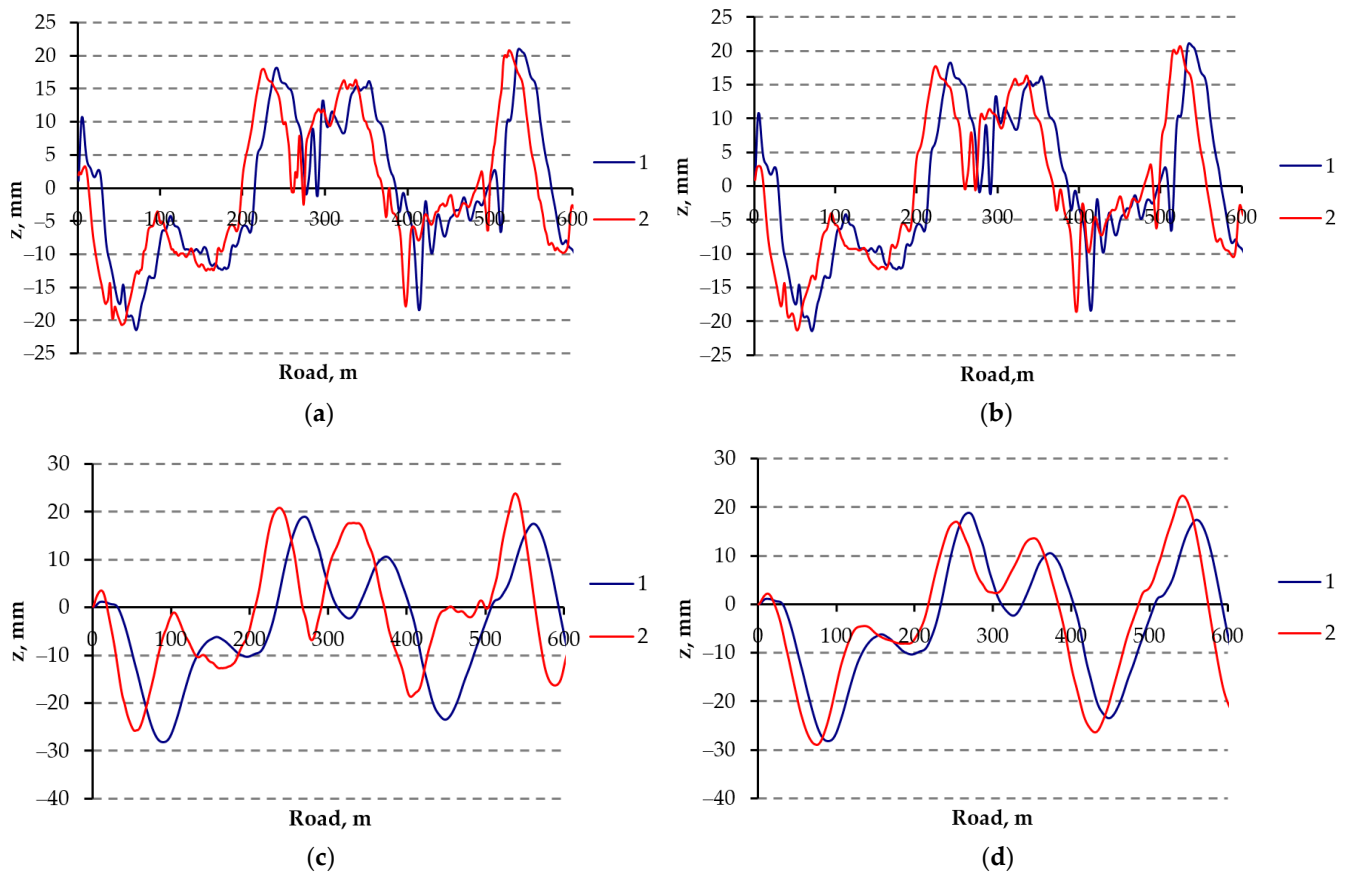


Figure 19. Displacements of unsprung (a,b) and sprung (c,d) masses (front) of the compact car, calculated using the quarter-car and 3D models: 1—quarter-car model; 2—3D model; (a,c)— $v = 40$ km/h; and (b,d)— $v = 80$ km/h.

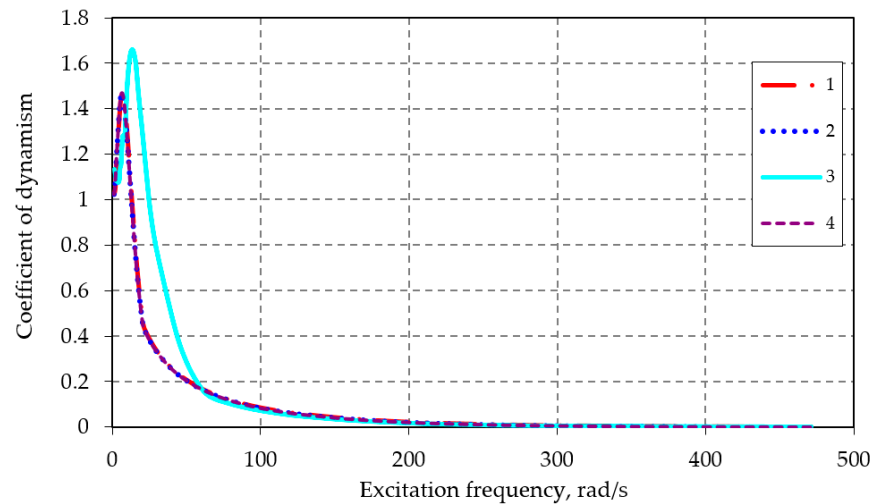
Table 6. Quarter-car and 3D model element characteristics.

Parameter	Quarter-Car Model	3D Model	
		Front	Rear
Sprung mass m_3 , kg	246	246	205
Unsprung mass m_2 , kg	27.5	27.5	32
Mass of the tire element m_1 , kg	0.3	0.3	0.3
Suspension spring stiffness c_3 , kN/m	18	18	24
Tire stiffness c_2 , kN/m	157	157	157
Tread stiffness c_1 , kN/m	15,000	15,000	15,000
Shock absorber damping k_3 , Ns/m	1835	1835	1835
Tire damping k_2 , Ns/m	475	475	475
Tread damping k_1 , Ns/m	0	0	0

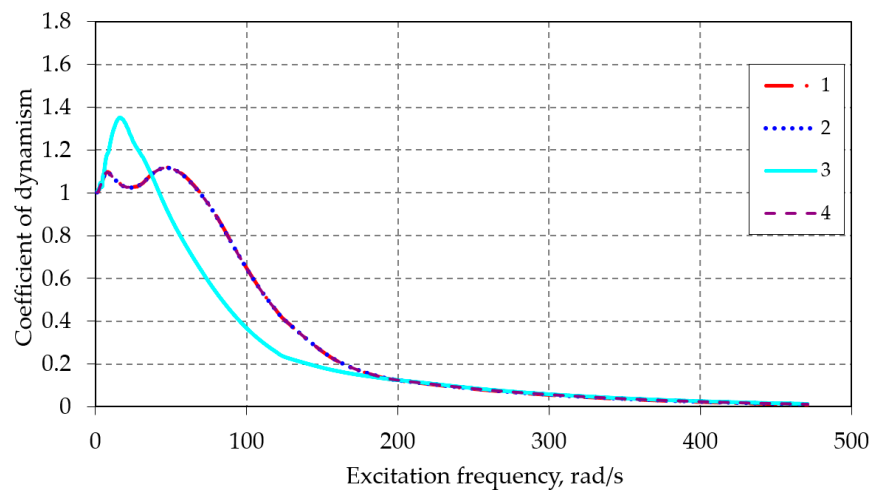
3.2. Excitation during Movement on the Asphalt Pavement

The influence of nonlinear characteristics of the elastic elements of suspension on the vertical displacements of the body and wheels caused by the excitation frequency was investigated during modeling of the stability of the compact car by combining different quality road profile and car speed, as well as assessing the influence of the tire tread. The results were compared by assessing the dependence of the coefficient of dynamism (ratio of sprung and unsprung mass displacements to the height of unevenness) on the road

excitation. Figure 20a,b shows the influence of nonlinear damping of shock absorbers and nonlinear stiffness of suspension on the sprung and unsprung mass displacements.



(a)

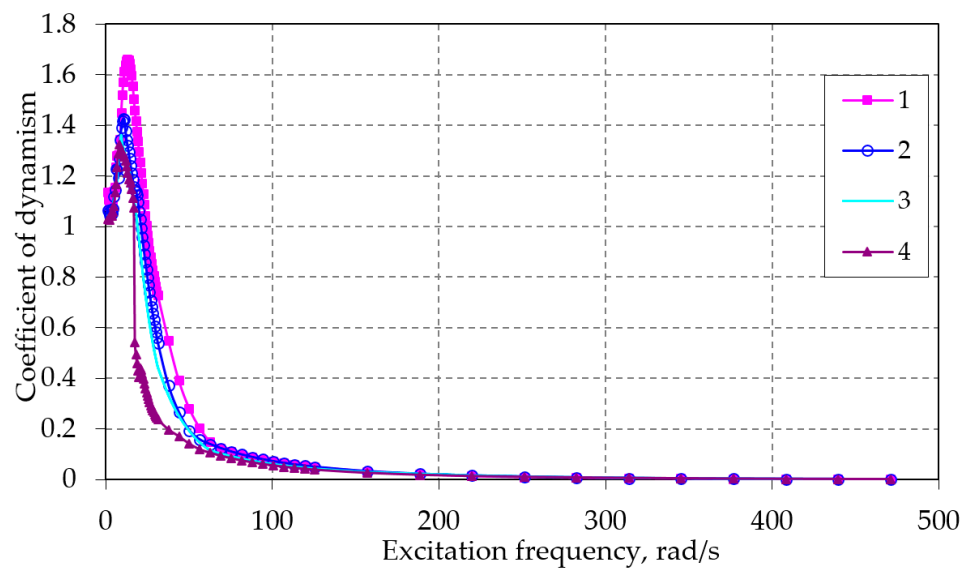


(b)

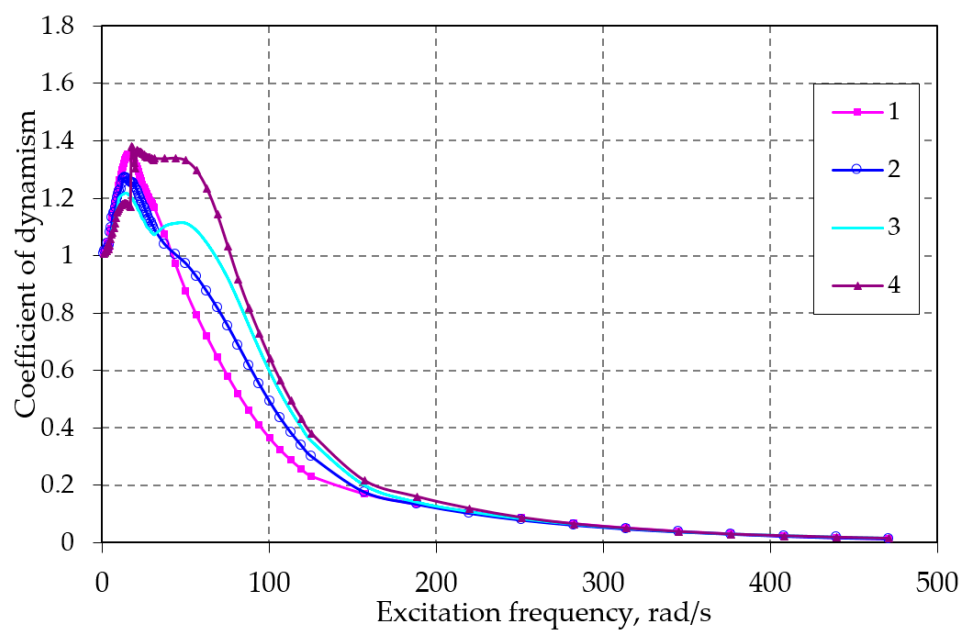
Figure 20. Influence of nonlinear damping of shock absorbers and nonlinear stiffness of suspension on the sprung (a) and unsprung (b) mass displacements: 1—linear shock absorber and linear suspension, tread not assessed; 2—tread assessed; 3—nonlinear shock absorber; and 4—nonlinear suspension.

With nonlinear elements, the frequency dependences shifted towards higher frequency because the damping of the shock absorbers due to nonlinearity increased suddenly, and the displacement (coefficient of dynamism) increased as well. The damping of the vibrations of the unsprung masses was fairly effective, but at a certain excitation frequency, the second peak would occur, causing certain damping deficiencies.

Figure 21a,b shows the influence of road unevenness on the tread displacements of the sprung and unsprung masses and the tire tread. As the unevenness increased, the coefficient of dynamism could be observed to increase as well. As long as the amplitude was small, the suspension and shock absorber would operate in a linear section. As the amplitude increased, the influence of the nonlinearity of the elements would be observed (Figure 21b).



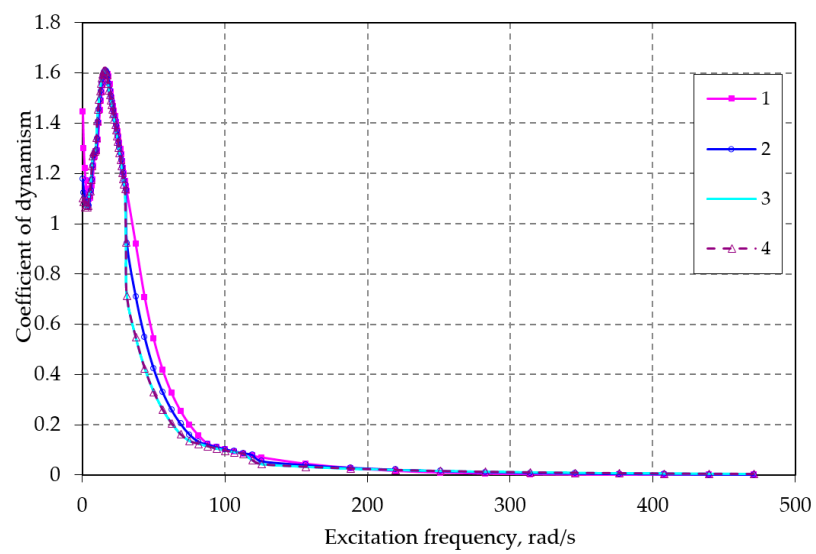
(a)



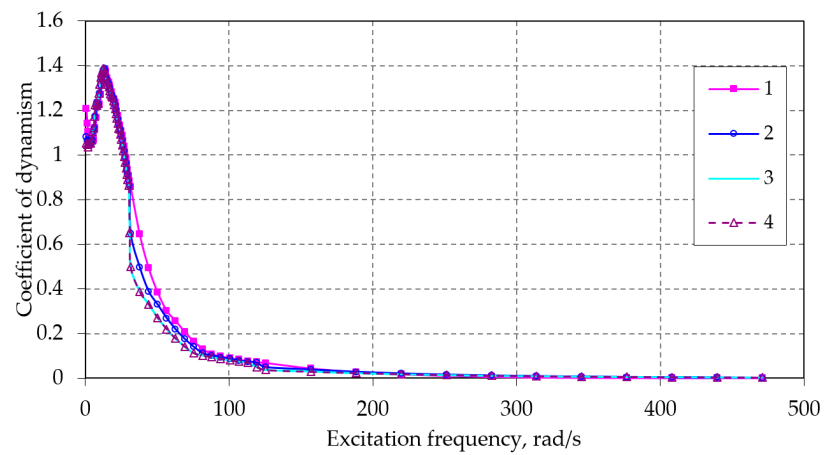
(b)

Figure 21. The influence of road unevenness on the sprung (a) and unsprung (b) mass displacements: 1—amplitude of irregularities 10.5 mm; 2—21 mm; 3—31.5 mm; and 4—42 mm.

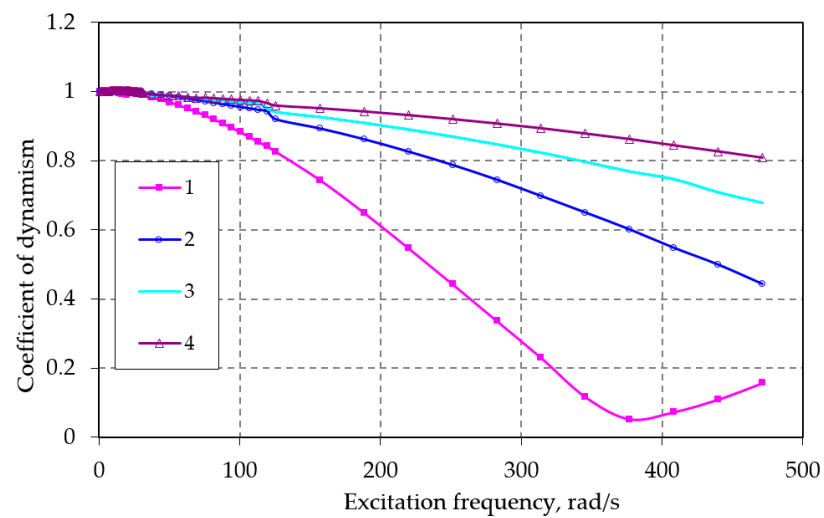
Figure 22a–c shows the influence of the car speed on the displacements of the sprung (body), unsprung (tire) masses, and tread displacements.



(a)



(b)



(c)

Figure 22. Influence of vehicle driving speed on the displacements of sprung mass (a), unsprung mass (b), and tire tread (c): 1—vehicle speed 10 m/s; 2—20 m/s; 3—30 m/s; and 4—40 m/s.

Damping of the sprung mass was effective at different speeds. The displacement reached its peak at low frequencies and afterward would decrease considerably. Tire deformations were the most sensitive to the effect of speed.

3.3. Experimental Investigation

In an investigation of a car stability, the characteristics of the road microprofile must be available. To measure the road microprofile, a measuring device consisting of the Volkswagen Transporter with DYNATEST road profile measuring equipment and laser sensors mounted on the front of the car were used (Figure 23).



Figure 23. Laser profilograph DYNATEST 5051 RSP mounted on the VW Transporter. Reprinted from ref. [58].

Measurement equipment: VAS-21 vibration analysis and processing system [59], PicoScope 3424 signal converter (Table 7), two low-frequency (WILCOXON Model 793L SN7688) and two medium-frequency (WILCOXON Model 784A SN12040) sensors (Table 8). The data were registered real-time on a PC, recorded, and processed using PICOSCOPE 5.13.7 software.

Table 7. Characteristics of the PicoScope 3424 signal converter. Reprinted from ref. [60].

Incoming signal values	± 20 mV to ± 20 V
Measured frequencies, max	10 MHz
Error	1%
Overload protection	± 100 V
Incoming signal values	1 M Ω in parallel to 20 pF
Input	BNC

Table 8. Sensor characteristics. Reprinted from ref. [61].

Characteristics	Sensor	
	WILCOXON Model 793L	WILCOXON Model 784A
Sensitivity, $\pm 20\%$, 25 °C	500 mV/g	100 mV/g
Measurement limits	± 10 g	± 50 g
Measured frequencies	0.6–700 Hz	4–7000 Hz
Supply voltage	18–30 V	18–30 V
Sensor mass	142 g	45 g

Measurements were performed in the city and on the highway. Road unevenness was measured using the Lithuanian Transport Safety Administration and Transport Competence Agency a VW Transporter car equipped with the measuring devices. The driving speeds in the city were and on the highway: 50, 60, 70, and 80 km/h. Measurement duration: 50 s.

To determine the frequency characteristics of the sprung and unsprung mass, compact car was selected for the study (Table 9).

Table 9. Compact car data.

Overall Dimensions, mm			Base, mm	Mass, kg		Tire Dimensions	Static Radius, mm	Tire Diameter, mm
Length	Width	Height		Tare	Payload			
3985	1665	1415	2475	870	1400	175/70R13	261	293

The measurement sensors for compact city car unsprung mass vibrations were mounted on the suspension arms (Figure 24a,b), while the sensors for measuring sprung mass vibrations were mounted on the front fender and car roof (Figure 24c,d).

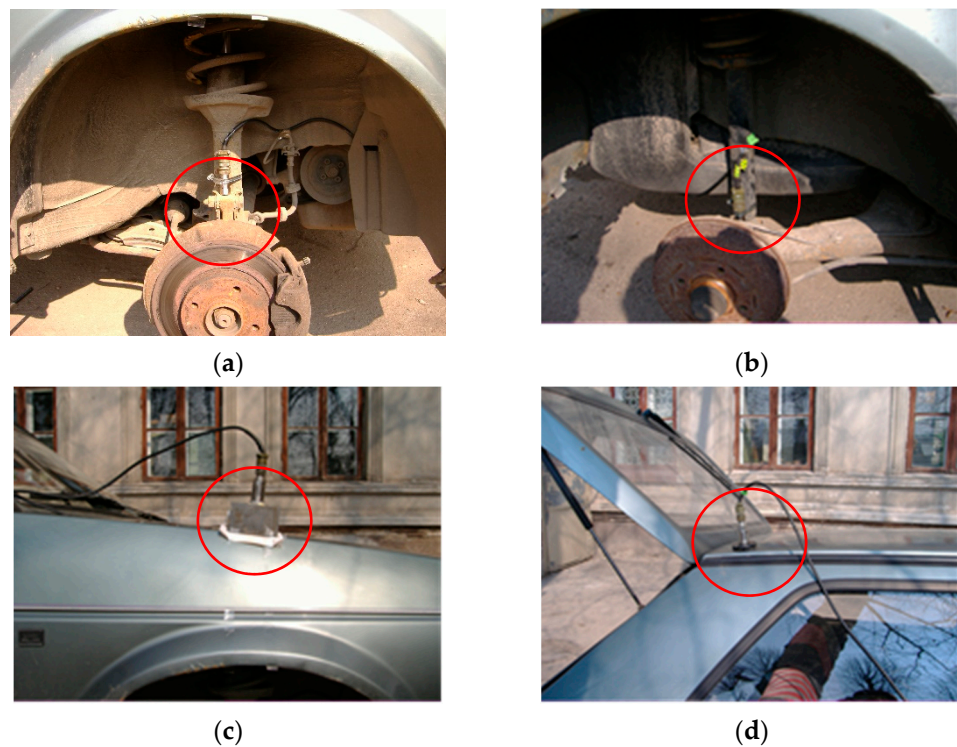


Figure 24. Mounting of sensors for measuring vibrations of unsprung mass: (a)—front suspension, (b)—rear suspension; and sprung mass: (c)—on the front fender, and (d)—on the roof.

During the experimental studies, the driving speed down the road of the investigated profile was different during the 50 s drive and the accelerations of the sprung (body) and unsprung (suspension) masses of the cars. The test results for the compact car are shown in Figures 25 and 26. High-intensity noise and the nonlinear reaction of the car suspension to excitation made the result analysis more complex. While the movements of the unsprung mass show relatively little variation at the speeds of 50 and 70 km/h, the reaction of the sprung mass was very different at the same speeds, as individual unevenness may excite considerable body displacements without causing any significant suspension deformations.

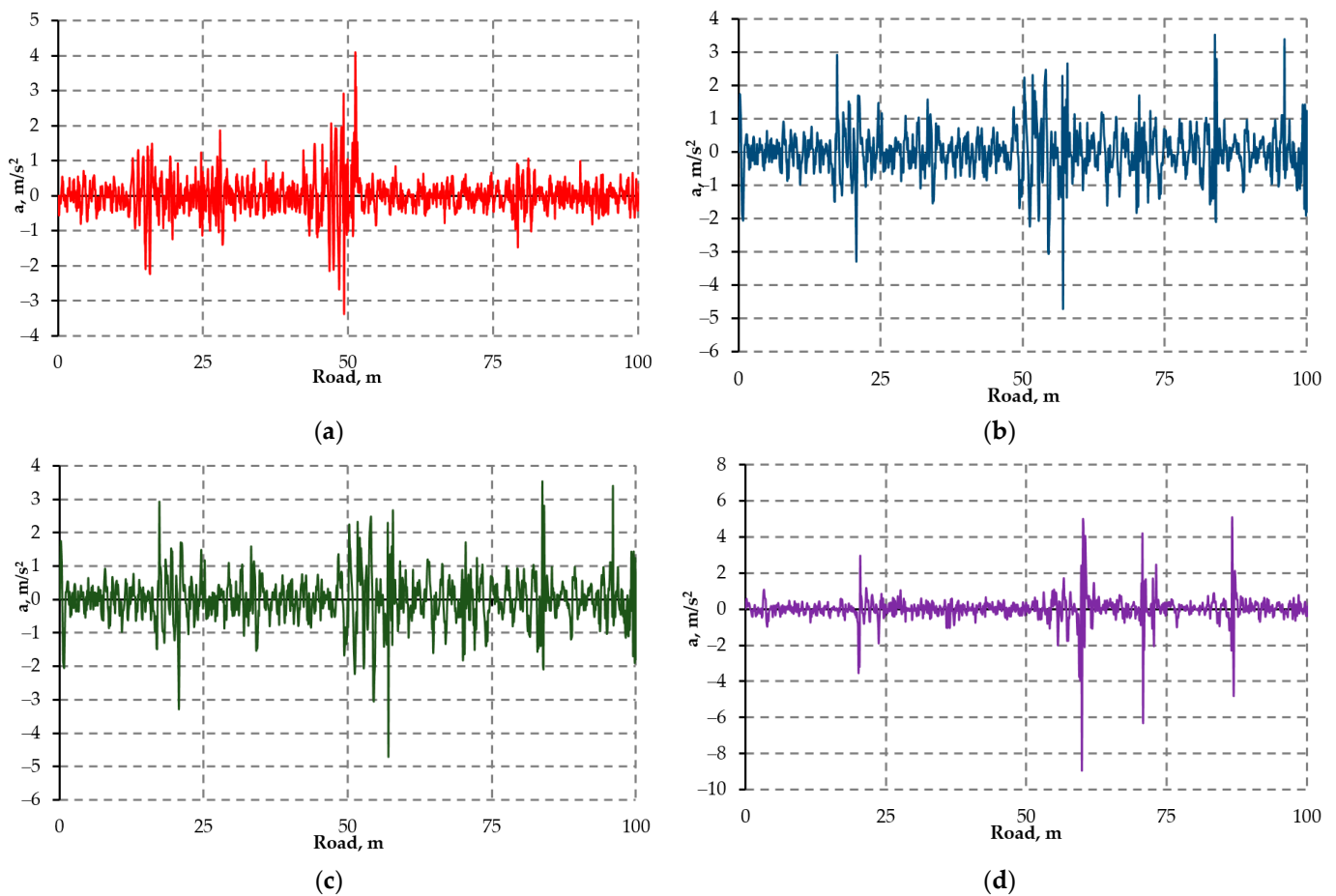


Figure 25. Accelerations of the sprung masses of compact car measured on a city-type road at different speeds: (a,b)—front; (c,d)—rear; (a,c)—50 km/h; and (b,d)—70 km/h.

Frequencies close to the frequency of own oscillations of the suspension (for passenger cars 0.8–1.3 Hz) and own oscillation frequency of unsprung masses (for passenger cars 8–13 Hz) were of particular interest in terms of the stability characteristic. It was the travel of the suspension that was defined as the difference between the displacements of the sprung and unsprung masses that had the greatest influence on the changes in the spatial position of the wheel. The equipment registered the peaks of the lowest frequencies in the range of 5–7 Hz (Figure 27), i.e., the frequencies characteristic of own oscillation frequency of the suspensions. In addition, the vibration sensors registered additional vibrations caused by the vibrations of the suspension elements (Figure 27a). Their frequencies exceeded the characteristic vibration frequencies of the tire (80–100 Hz). The oscillations were transmitted to the body (Figure 27b); however, comparing the frequency spectra of sprung and unsprung masses, the oscillations in the body were observed to be influenced by the structure of elements selected as sensor mounting points, namely, the wing at the suspension fixing point was less sensitive to high-frequency vibrations than the roof panel.

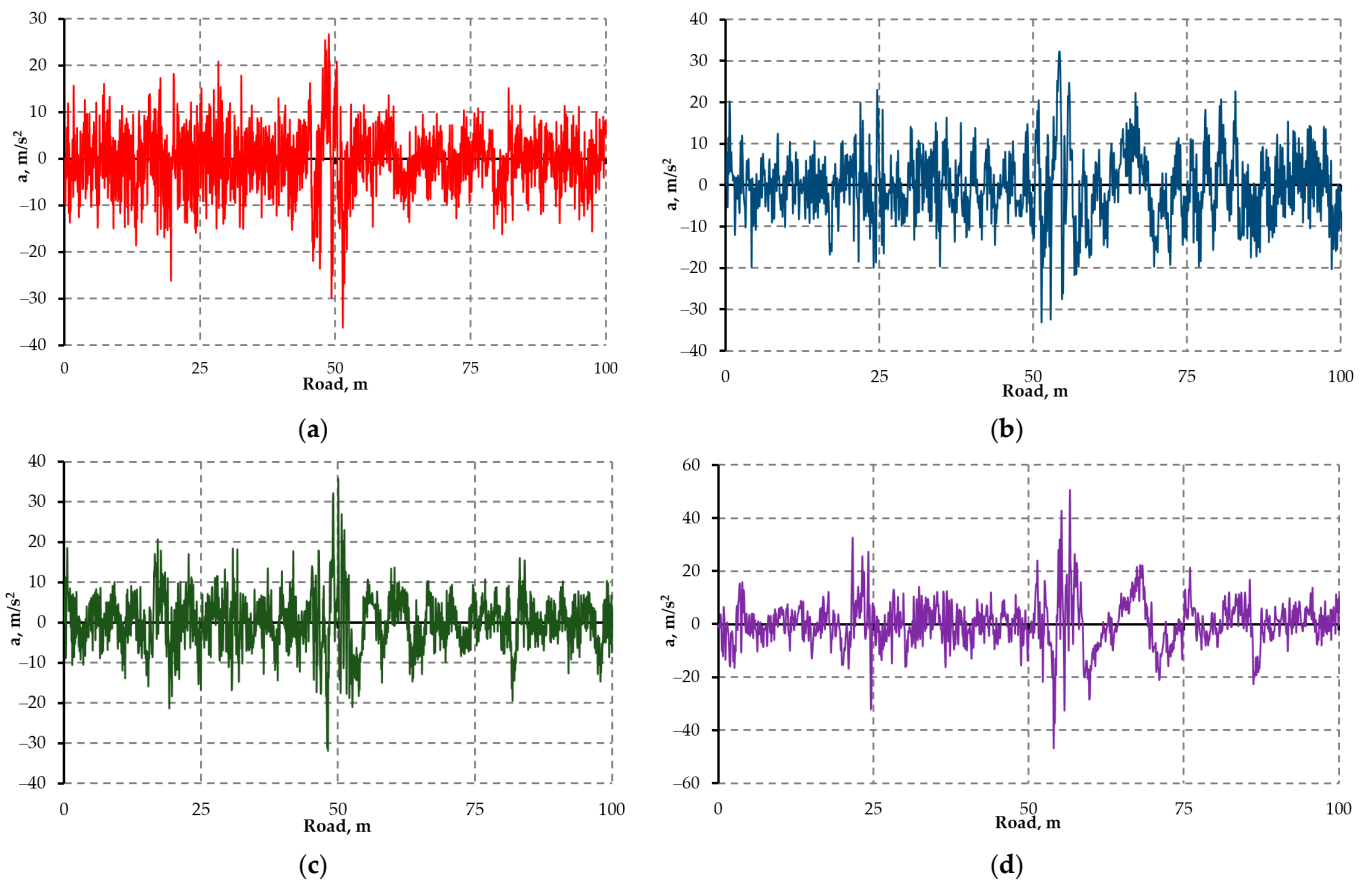


Figure 26. Accelerations of the unsprung masses of compact car measured on a city-type road at different speeds: (a,b)—front; (c,d)—rear; (a,c)—50 km/h; and (b,d)—70 km/h.

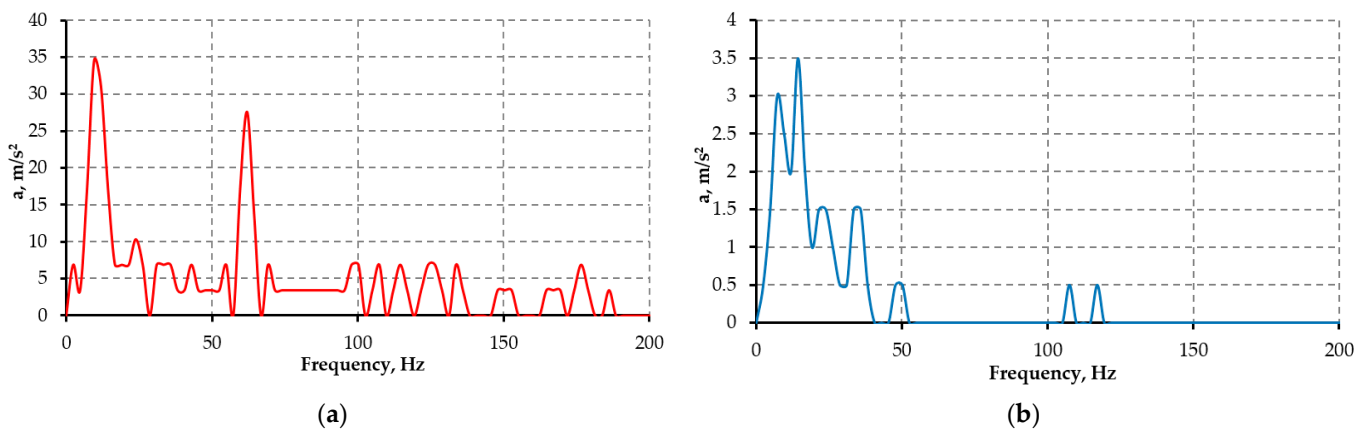


Figure 27. Frequency spectra of compact car on city type road at the speed of 70 km/h: (a)—front, unsprung mass and (b)—front, sprung mass.

The aim of the experiment was to verify the modeling results and investigate their applicability to stability analysis. A Fourier series was used for frequency analysis of the results of direct measurements used for further studies (Figure 27). The Fourier analysis provides a wider spectrum but also does not highlight the characteristic body—and suspension-specific frequencies. This may be related to the specifics of the road. Further research identified how the results of simulation of the suspension operation could be used to define stability.

3.4. Comparison of Excitation from Road Unevenness and Experimental Study

During the modeling, it was assumed that the compact car was moving on a road of a known profile in the city and on the highway at the speed of 50, 60, 70, and 80 km/h. To compare the results of modeling and experiment, a 100 m long road section was used. Road unevenness of the examined section was measured using profilograph DYNATEST 5051 RSP. The vehicle and suspension data used for the modeling are presented in Table 7. Matlab program (3D model with nonlinear suspension elements) was used for the modeling. The modeling results are presented in Figures 28–30.

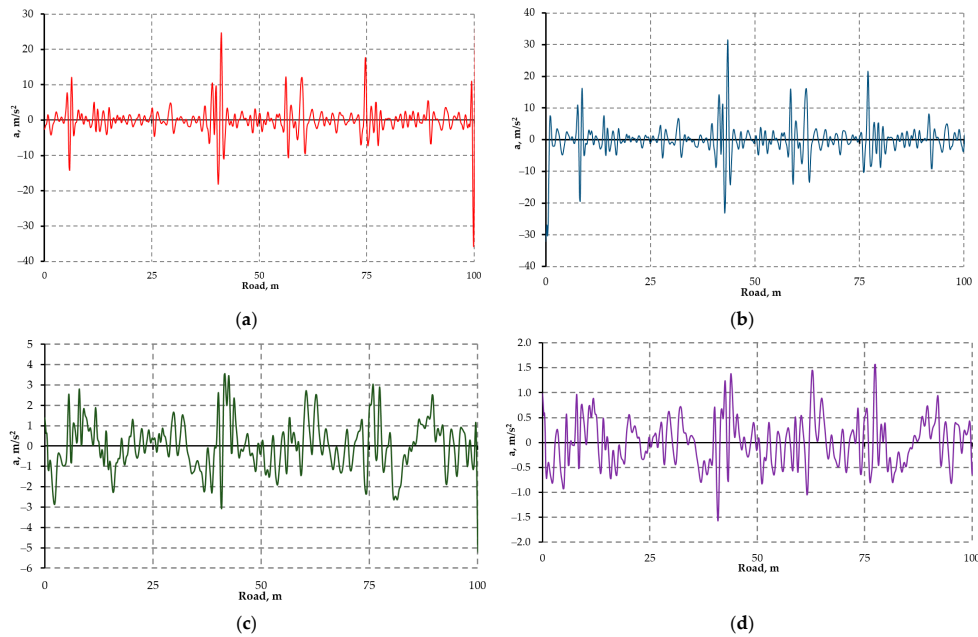


Figure 28. Accelerations of the unsprung (a,b) and sprung (c,d) masses of compact city measured by modeling on a city-type road at 50 km/h speed: (a,c)—front and (b,d)—rear.

Comparison of the curves of experimental and numerical modeling results suggested that in both cases very similar acceleration values were obtained (acceleration peak values differed by 5–7% for sprung masses and 20–25% for unsprung masses). Comparison of the dependences of accelerations by means of Fourier analysis (Figure 29) with the experimental results suggested that a share of the vibrations caused by the resonance and stability of the suspension and body parts may be omitted from the assessment in the research findings.

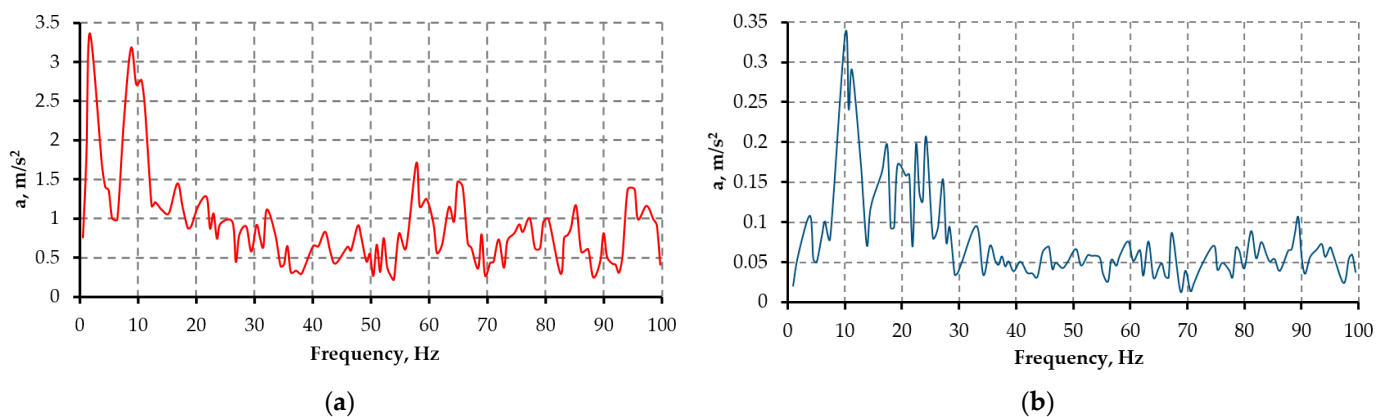


Figure 29. Frequency dependence of amplitudes of compact city, obtained by Fourier analysis: (a)—front damped unsprung mass and (b)—front damped sprung mass (city-type road, $v = 70$ km/h).

The obtained results show that the recording and analysis of signals required for active suspensions is an area of separate studies, as the additional noise and signal sources were recorded during the experiment, which also interfered with the analysis of directional stability. Therefore, the differences between the displacements of the sprung and unsprung masses were examined for further analysis (Figure 30). The maximum amplitude of the difference between the suspension and body displacements was 47 mm for the experiment and 40 mm for the modeling.

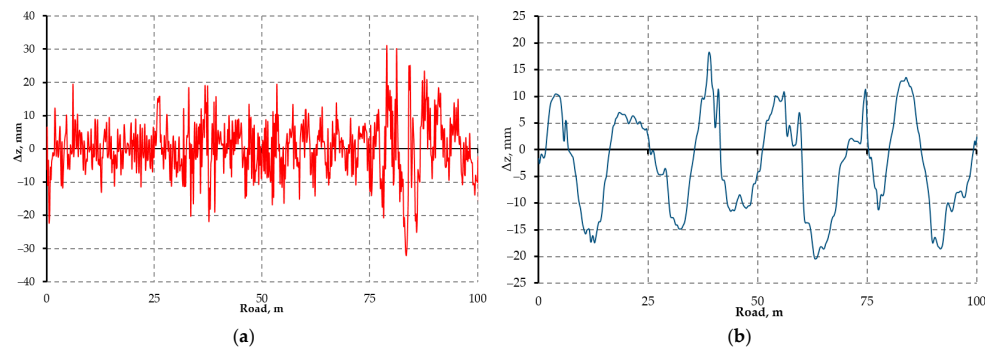


Figure 30. Difference between the sprung and unsprung mass displacements Δz simulating driving at the speed of 70 km/h: (a)—experiment and (b)—model.

4. Discussion

The analysis of the tire tread as the elastic band model using the numerical models has shown that due to the specificity of rubber deformability, the cord and breaker layers have effect on its stiffness in the radial direction by restricting the tread deformations.

The experiment confirmed the theoretical assumptions and showed that the reduced modulus of elasticity of the tread was 4.5 times higher than the modulus of elasticity of the tread material.

It was found that when assessing the tread deformation for different types of tires, summative expressions could be used for the relative coordinates as they use the relative load determined on the basis of the nominal tire load, thus greatly simplifying the assessment of tire deformation.

The analysis of the interaction between the tread and the road texture showed that the tread would even out the unevenness in the texture level, but the depressions would not be completely filled, thereby ensuring better adhesion between the tire and the road.

The specifics of the tire in the road-to-car interaction were determined. The deformation characteristics of the tread in the radial direction did not depend much on the tire or, consequently, on the type of vehicle.

Comparison of the quarter-car and 3D models showed that more detailed information necessary for stability assessment was provided by the 3D model, which predicted the sprung mass displacements higher by up to 20%.

The results of the experiment on the asphalt pavement were compared with the model. Certain issues were observed in the analysis of experimental results due to additional oscillations and vibrations occurring in the body and suspension elements, which could be avoided by modeling the movement after recording the road microprofile with a profilograph. The parameters that have the greatest impact on the stability of the direction—the difference between the displacement of the sprung and unsprung masses in the model versus the field experiment—did not exceed 15%.

Further Investigations

Based on the tire deformation properties obtained in this paper, numerically and experimentally investigated vertical excitation results, the changes in wheel position due to road roughness during suspension excitation can be determined and an analysis of the

vehicle's yaw process can be performed. The modeling of the vehicle's directional stability needs to consider the specifics of the suspensions, such as the redistribution of radial loads under lateral force and the changes in wheel geometry due to the kinematic properties of the suspension. The obtained results justify further refinements of the directional stability numerical models:

- development of a dynamic model of a comprehensive integrated assessment of the suspension characteristics, suspension kinematics, steering mechanism, and pavement condition. The model would provide the development of a methodology for determination of the vehicles handling characteristics on roads of known quality using the numerical models.
- investigation of the sensitivity of the individual suspension types to vertical excitation in terms of directional stability criteria and to evaluate the technical condition of the vehicle if the tendency of changes in suspension parameters during known operation. To evaluate the technical condition of the vehicle by modifying the stiffness of the suspension components.
- analysis of vehicle stability in cornering, taking into account the changing position of the wheels as the vehicle is steered, which may have an effect on the vehicle stability. The stability of a vehicle in a turning situation requires the consideration of two criteria: the loss of stability of the vehicle when skidding, and the loss of stability of the vehicle when overturning. In addition, it is necessary to specify the effect of changes in the vehicle's trajectory in a corner due to the deformation of the suspension and the changes in the position of the wheels as the vehicle is steered.
- integrating driver reactions into the vehicle stability model. Without a driver model, such a simulation is not effective, as the vehicle model changes direction due to random effects and requires frequent correction to simulate steering course corrections.

5. Conclusions

1. The revised model of the tire equalizing function was developed. The coordinates of relative measures were found to cause no essential difference in assessment of tire deformations of different vehicle tires. This means that the number of tire groups may be reduced for assessment of their impact on stability.
2. The tread deformation characteristics of the tire were investigated by numerical modeling and experiment and showed that the tread deformations could be assessed by simplified models instead of the modulus of elasticity of the tread material, $E_r = 6$ MPa using the calculated modulus of elasticity $E_{1z} = 27$ MPa.
3. Studies on different types of cars (passenger cars, light-duty trucks and SUVs) have shown that the 3D suspension models more accurately provide reflection of the real situation in terms of stability assessment, while simpler quarter-car models can be used for comfort assessment. Comparison of the quarter-car model with the 3D model has shown that, in case of the latter, the resulting wheel travel is higher by up to 20%.
4. The results of the experiment on the asphalt pavement were compared with the model. Certain issues were observed in the analysis of experimental results due to additional oscillations and vibrations occurring in the body and suspension elements, which could be avoided by modeling the movement after recording the road microprofile with a profilograph. The parameters that have the greatest impact on the stability of the direction—the difference between the displacement of the sprung and unsprung masses in the model versus the field experiment—did not exceed 15%.
5. Changes in the car behavior at changing speed are related not only to the slip effect but also to changes in the wheel spatial position due to the suspension kinematics and suspension incompatibility with the steering mechanism. This effect can be particularly pronounced when road defects (pits, ruts) lead to an increase in the suspension travel.

Author Contributions: Conceptualization, V.L., R.M. and A.D.; methodology, V.L., R.M. and A.D.; software, V.L., R.M. and A.D.; validation, V.L., R.M. and A.D.; formal analysis, V.L., R.M. and A.D.; investigation, V.L., R.M. and A.D.; resources, V.L., R.M. and A.D.; data curation, V.L., R.M. and A.D.; writing—original draft preparation, V.L., R.M. and A.D.; writing—review and editing, V.L., R.M. and A.D.; visualization, V.L., R.M. and A.D.; supervision, V.L., R.M. and A.D.; project administration, V.L., R.M. and A.D.; funding acquisition, V.L., R.M. and A.D. All authors have read and agreed to the published version of the manuscript.

Funding: This research received no external funding.

Institutional Review Board Statement: Not applicable.

Informed Consent Statement: Not applicable.

Data Availability Statement: Not applicable.

Conflicts of Interest: The authors declare no conflict of interest.

References

- Misaghi, S.; Tirado, C.; Nazarian, S.; Carrasco, C. Impact of pavement roughness and suspension systems on vehicle dynamic loads on flexible pavements. *Transp. Eng.* **2021**, *3*, 100045. [CrossRef]
- Mahajan, G.R.; Radhika, B.; Biligiri, K.P. A critical review of vehicle-pavement interaction mechanism in evaluating flexible pavement performance characteristics. *Road Mater. Pavement Des.* **2020**. [CrossRef]
- Zoccali, P.; Loprencipe, G.; Lupascu, R.C. Acceleration measurements inside vehicles: Passengers' comfort mapping on railways. *Measurement* **2018**, *129*, 489–498. [CrossRef]
- Rill, G.; Castro, A. *Road Vehicle Dynamics: Fundamentals and Modeling with MATLAB*, 2nd ed.; CRC Press: Boca Raton, FL, USA, 2020. [CrossRef]
- Yechen, Q.; Hong, W.; Huang, Y.; Xiaolin, T. *Real-Time Road Profile Identification and Monitoring: Theory and Application*; Morgan & cLaypool Publishers: San Rafael, CA, USA, 2019. [CrossRef]
- Yang, S.; Chen, L.; Li, S. *Dynamics of Vehicle-Road Coupled System*; Springer: Beijing, China, 2015.
- Leitner, B.; Decký, M.; Kováč, M. Road pavement longitudinal evenness quantification as stationary stochastic process. *Transport* **2019**, *34*, 195–203. [CrossRef]
- Loprencipe, G.; Zoccali, P.; Cantisani, G. Effects of Vehicular Speed on the Assessment of Pavement Road Roughness. *Appl. Sci.* **2019**, *9*, 1783. [CrossRef]
- Yan, J.; Zhang, H.; Hui, B. Driving Safety Analysis Using Grid-Based Water-Filled Rut Depth Distribution. *Adv. Mater. Sci. Eng.* **2021**, 5568949. [CrossRef]
- Yan, J.; Zhang, H.; Hui, B. Analysis of the lateral slope's impact on the calculation of water-filled rut depth. *PLoS ONE* **2020**, *15*, e0243952. [CrossRef]
- Ružinskas, A.; Giessler, M.; Gauterin, F.; Wiese, K.; Bogdevičius, M. Experimental investigation of tire performance on slush. *Eksploat. I Niezawodn. Maint. Reliab.* **2021**, *23*, 103–109. [CrossRef]
- Gogoi, R.; Das, A.; Chakroborty, P. Rut depth measurement of an asphalt pavement from its original profile. *Aust. J. Civ. Eng.* **2020**, *18*, 119–125. [CrossRef]
- Zhang, Z.; Sun, C.; Sun, M.; Bridgelall, R. Application of a Machine Learning Method to Evaluate Road Roughness from Connected Vehicles. *J. Transp. Eng. Part B Pavements* **2018**, *144*, 04018043. [CrossRef]
- Zhang, Z.; Sun, C.; Bridgelall, R.; Sun, M. Road profile reconstruction using connected vehicle responses and wavelet analysis. *J. Terramech.* **2018**, *80*, 21–30. [CrossRef]
- Hussan, S.; Kamal, M.A.; Hafeez, I.; Ahmad, N.; Khanzada, S.; Ahmed, S. Modelling asphalt pavement analyzer rut depth using different statistical techniques. *Road Mater. Pavement Des.* **2020**, *21*, 117–142. [CrossRef]
- Prażnowski, K.; Mamala, J.; Śmieja, M.; Kupina, M. Assessment of the Road Surface Condition with Longitudinal Acceleration Signal of the Car Body. *Sensors* **2020**, *20*, 5987. [CrossRef] [PubMed]
- Lenkutis, T.; Čerškus, A.; Šešok, N.; Dzedzickis, A.; Bučinskis, V. Road Surface Profile Synthesis: Assessment of Suitability for Simulation. *Symmetry* **2021**, *13*, 68. [CrossRef]
- Pacejka, H.B.; Besselink, I. *Tire and Vehicle Dynamics*, 3rd ed.; Butterworth-Heinemann: Oxford, UK, 2012. Available online: http://scholar.google.com/scholar_lookup?hl=en&publication_year=2012&author=HB+Pacejka&author=I.+Besselink&title=Tire+and+vehicle+dynamics (accessed on 5 January 2021).
- Shaohua, L. *Dynamics of Vehicle-Road Coupled System*; Science Press: Beijing, China; Springer: Heidelberg/Berlin, Germany, 2015. Available online: https://scholar.google.lt/scholar?hl=lt&as_sdt=0%2C5&q=Dynamics+of+Vehicle%E2%80%93Road+Coupled+System&btnG (accessed on 10 March 2021).
- Mavromatis, S.; Laiou, A.; Yannis, G. Safety assessment of control design parameters through vehicle dynamics model. *Accid. Anal. Prev.* **2019**, *125*, 330–335. [CrossRef] [PubMed]

21. Yin, Y.; Wen, H.; Sun, L.; Hou, W. Study on the Influence of Road Geometry on Vehicle Lateral Instability. *J. Adv. Transp.* **2020**, 7943739. [[CrossRef](#)]
22. Saeedi, M.A. Simultaneous improvement of handling and lateral stability via a new robust control system. *Mech. Based Des. Struct. Mach.* **2021**. [[CrossRef](#)]
23. Vijaykumar, V.; Anand, P. Design Optimization of Suspension and Steering Systems for Commercial Vehicles. In Proceedings of the ICDMC 2019, Chennai, India, 28–29 March 2019; Lecture Notes in Mechanical Engineering. Yang, L.J., Haq, A., Nagarajan, L., Eds.; Springer: Singapore, 2020. [[CrossRef](#)]
24. Cheng, S.; Li, L.; Yan, B.; Liu, C.; Wang, X.; Fang, J. Simultaneous estimation of tire side-slip angle and lateral tire force for vehicle lateral stability control. *Mech. Syst. Signal Process.* **2019**, 132, 168–182. [[CrossRef](#)]
25. Joa, E.; Yi, K.; Hyun, Y. Estimation of the tire slip angle under various road conditions without tire–road information for vehicle stability control. *Control. Eng. Pract.* **2019**, 86, 129–143. [[CrossRef](#)]
26. Huang, Y.; Liang, W.; Chen, Y. Estimation and analysis of vehicle lateral stability region. In Proceedings of the American Control Conference (ACC), Seattle, WA, USA, 24–26 May 2017; pp. 4303–4308. [[CrossRef](#)]
27. Zhang, X.; Wang, P.; Li, Z.; Wang, F.; Chen, H. Estimation and Analysis of Vehicle Stability Region under Complex Road Conditions. In Proceedings of the Chinese Automation Congress (CAC), Shanghai, China, 6–8 November 2020; pp. 3036–3041. [[CrossRef](#)]
28. Xu, N.; Huang, Y.; Askari, H.; Tang, Z. Tire Slip Angle Estimation Based on the Intelligent Tire Technology. *IEEE Trans. Veh. Technol.* **2021**, 70, 2239–2249. [[CrossRef](#)]
29. Cheli, F.; Sabbioni, E.; Pesce, M.; Melzi, S. A methodology for vehicle side slip angle identification: Comparison with experimental data. *Veh. Syst. Dyn.* **2007**, 45, 549–563. [[CrossRef](#)]
30. Shekh, M.; Umrao, O.P.; Singh, D. Kinematic Analysis of Steering Mechanism: A Review. In Proceedings of the International Conference in Mechanical and Energy Technology. Smart Innovation, Systems and Technologies, Greater Noida, India, 7–8 November 2019; Yadav, S., Singh, D., Arora, P., Kumar, H., Eds.; Springer: Singapore, 2019; Volume 174. [[CrossRef](#)]
31. Pradhan, D.; Ganguly, K.; Swain, B.; Roy, H. Optimal kinematic synthesis of 6 bar rack and pinion Ackerman steering linkage. *Proc. Inst. Mech. Eng. Part D J. Automob. Eng.* **2021**, 235, 1660–1669. [[CrossRef](#)]
32. Lv, T.; Zhang, Y.; Duan, Y.; Yang, J. Kinematics & compliance analysis of double wishbone air suspension with frictions and joint clearances. *Mech. Mach. Theory* **2021**, 156, 104127. [[CrossRef](#)]
33. von Wysocki, T.; Chahkar, J.; Gauterin, F. Small Changes in Vehicle Suspension Layouts Could Reduce Interior Road Noise. *Vehicles* **2020**, 2, 18–34. [[CrossRef](#)]
34. Ciampaglia, A.; Santini, A.; Belingardi, G. Design and analysis of automotive lightweight materials suspension based on finite element analysis. *Proc. Inst. Mech. Eng. Part C J. Mech. Eng. Sci.* **2021**, 235, 1501–1511. [[CrossRef](#)]
35. Böhm, F. Dynamic rolling process of tires as layered structures. *Mech. Compos. Mater.* **1996**, 32, 568–576. [[CrossRef](#)]
36. Sapragnas, J.; Dargužis, A. Model of radial deformations of protector of vehicle tire. *Mechanics* **2011**, 17, 21–29. [[CrossRef](#)]
37. Sapragnas, J.; Keršys, A.; Makaras, R.; Lukoševičius, V.; Juodvalkis, D. Research of the influence of tire hydroplaning on directional stability of vehicle. *Transport* **2013**, 28, 374–380. [[CrossRef](#)]
38. Levin, M.A.; Fufaev, N.A. *Theory of Deformable Wheel Rolling*; Nauka: Moscow, Russia, 1989. (In Russian)
39. Berthelot, J.M. *Matériaux Composites*, 5th ed.; Masson: France, Paris, 2012; (In French). Available online: https://scholar.google.com/scholar_lookup?author=M.+Berthelot&journal=Mat%C3%A9riaux+Composites.+Comportement+m%C3%A9canique+et+analyse+des+structures&publication_year=1999 (accessed on 15 July 2020).
40. Sharma, S. *Composite Materials*, 1st ed.; CRC Press: New York, NY, USA, 2021.
41. Cristensen, R.M. *Mechanics of Composite Materials*; Dover Publications, Inc.: New York, NY, USA, 2005.
42. Gay, D. *Matériaux Composites*; Hermes: Paris, France, 1997; Available online: https://scholar.google.com/scholar_lookup?author=D.+Gay&journal=Mat%C3%A9riaux+Composites&publication_year=1997 (accessed on 15 July 2020).
43. Pakalnis, A. Investigation of elasticity characteristics in a tyre ring model. *Mechanics* **2000**, 3, 59–62.
44. Hilyard, N.C. *Mechanics of Cellular Plastics*; Macmillan: New York, NY, USA, 1982.
45. Matlin, M.; Kazankina, E.; Kazankin, V. Mechanics of initial dot contact. *Mechanics* **2009**, 76, 20–23. Available online: <https://web.a.ebscohost.com/ehost/pdfviewer/pdfviewer?vid=0&sid=412aad69-e974-47ff-ab94-820fa51cb935%40sdc-v-sessmgr01> (accessed on 15 March 2021).
46. Haddar, M.; Chaari, R.; Baslamisli, S.C.; Chaari, F.; Haddar, M. Intelligent optimal controller design applied to quarter car model based on non-asymptotic observer for improved vehicle dynamics. *Proc. Inst. Mech. Eng. Part I J. Syst. Control Eng.* **2021**, 235, 929–942. [[CrossRef](#)]
47. Negash, B.A.; You, W.; Lee, J.; Lee, C.; Lee, K. Semi-active control of a nonlinear quarter-car model of hyperloop capsule vehicle with Skyhook and Mixed Skyhook-Acceleration Driven Damper controller. *Adv. Mech. Eng.* **2021**. [[CrossRef](#)]
48. Jain, S.; Saboo, S.; Pruncu, C.I.; Unune, D.R. Performance Investigation of Integrated Model of Quarter Car Semi-Active Seat Suspension with Human Model. *Appl. Sci.* **2020**, 10, 3185. [[CrossRef](#)]
49. Filipozzi, L.; Assadian, F.; Kuang, M.; Johri, R.; Velazquez Alcantar, J. Estimation of Tire Normal Forces including Suspension Dynamics. *Energies* **2021**, 14, 2378. [[CrossRef](#)]
50. Aljarbouh, A.; Fayaz, M. Hybrid Modelling and Sliding Mode Control of Semi-Active Suspension Systems for Both Ride Comfort and Road-Holding. *Symmetry* **2020**, 12, 1286. [[CrossRef](#)]

51. Shahid, Y.; Wei, M. Comparative Analysis of Different Model-Based Controllers Using Active Vehicle Suspension System. *Algorithms* **2020**, *13*, 10. [[CrossRef](#)]
52. Khan, M.A.; Abid, M.; Ahmed, N.; Wadood, A.; Park, H. Nonlinear Control Design of a Half-Car Model Using Feedback Linearization and an LQR Controller. *Appl. Sci.* **2020**, *10*, 3075. [[CrossRef](#)]
53. Ahmad, E.; Iqbal, J.; Arshad Khan, M.; Liang, W.; Youn, I. Predictive Control Using Active Aerodynamic Surfaces to Improve Ride Quality of a Vehicle. *Electronics* **2020**, *9*, 1463. [[CrossRef](#)]
54. Zhang, Q.; Hou, J.; Duan, Z.; Jankowski, Ł.; Hu, X. Road Roughness Estimation Based on the Vehicle Frequency Response Function. *Actuators* **2021**, *10*, 89. [[CrossRef](#)]
55. Perrelli, M.; Farroni, F.; Timpone, F.; Mundo, D. Analysis of Tire Temperature Influence on Vehicle Dynamic Behaviour Using a 15 DOF Lumped-Parameter Full-Car Model. In *Advances in Service and Industrial Robotics; Mechanisms and Machine Science*; Zeghloul, S., Laribi, M., Sandoval Arevalo, J., Eds.; Springer: Cham, Switzerland, 2020; Volume 84. [[CrossRef](#)]
56. Mei, T.; Vanliem, N. Control performance of suspension system of cars with PID control based on 3D dynamic model. *J. Mech. Eng. Autom. Control. Syst.* **2020**, *1*, 1–10. [[CrossRef](#)]
57. Blekhman, I.; Kremer, E. Vertical-longitudinal dynamics of vehicle on road with unevenness. *Procedia Eng.* **2019**, *199*, 3278–3283. [[CrossRef](#)]
58. Dimaitis, M. *Modern Technologies for Evaluating the Condition of Road Surfaces*; Ex Arte: Vilnius, Lithuania, 2008; pp. 32–35. (In Lithuanian)
59. *Vibration Processing Collection and Analysis System VAS–21. User Guide*; UAB Elintos Prietaisai: Kaunas, Lithuania, 2003. (In Lithuanian)
60. PicoScope 3000 Series High-Performance Oscilloscopes. Available online: <http://www.picotech.com/picoscope3000.html> (accessed on 15 July 2020).
61. Wilcoxon Low Frequency Accelerometers. Available online: <http://www.wilcoxon.com> (accessed on 15 July 2020).